U-Pb ages of secondary silica at Yucca Mountain, Nevada: Implications for the paleohydrology of the unsaturated zone

L.A. Neymark[a*], Y. Amelin[b], J.B. Paces[c], Z.E. Peterman[c]

[a]*Pacific Western Technologies, Ltd., c/o U.S. Geological Survey, Denver Federal Center, Box 25046, MS 963, Denver, CO 80225, USA*

[b]*Jack Satterly Geochronology Laboratory, Royal Ontario Museum, 100 Queen's Park, Toronto, Ontario, M5S 2C6, Canada*

[c]*U.S. Geological Survey, Denver Federal Center, Box 25046, MS 963, Denver, CO 80225, USA*

[*]Corresponding author:
Tel: (303) 236-7898
Fax: (303) 236-4930
E-mail address: lneymark@usgs.gov

Abstract

U, Th, and Pb isotopes were analyzed in layers of opal and chalcedony from individual millimeter- to centimeter-thick calcite and silica coatings at Yucca Mountain, Nevada, USA, a site that is being evaluated for a potential high-level nuclear waste repository. These calcite and silica coatings on fractures and in lithophysal cavities in Miocene-age tuffs in the unsaturated zone (UZ) precipitated from descending water and record a long history of percolation through the UZ. Opal and chalcedony have high concentrations of U (10 to 780 ppm) and low concentrations of common Pb as indicated by large values of $^{206}Pb/^{204}Pb$ (up to 53,806), thus making them suitable for U-Pb age determinations.

Interpretations of U-Pb isotopes in opal samples at Yucca Mountain are complicated by the incorporation of excess ^{234}U at the time of mineral formation, resulting in reverse discordance of U-Pb ages. However, the $^{207}Pb/^{235}U$ ages are much less affected by deviation from initial secular equilibrium and provide reliable ages of most silica deposits between 0.6 and 9.8 Ma. For chalcedony subsamples showing normal age discordance, these ages may represent minimum times of deposition. Typically, $^{207}Pb/^{235}U$ ages are consistent with the microstratigraphy in the mineral coating samples, such that the youngest ages are for subsamples from outer layers, intermediate ages are from inner layers, and oldest ages are from innermost layers. ^{234}U and ^{230}Th in most silica layers deeper in the coatings are in secular equilibrium with ^{238}U, which is consistent with their old age and closed system behavior during the past 0.5 m.y.

U-Pb ages for subsamples of silica layers from different microstratigraphic positions in individual calcite and silica coating samples collected from lithophysal cavities in the welded part of the Topopah Spring Tuff yield slow long-term average depositional rates of 1 to 5 mm/m.y. These data imply that the deeper parts of the UZ at Yucca Mountain maintained long-term hydrologic stability over the past 10 m.y. despite significant climate variations. U-Pb ages for subsamples of silica layers from different microstratigraphic positions in individual calcite

and silica coating samples collected from fractures in the welded part of the overlying Tiva Canyon Tuff indicate larger long-term average depositional rates up to 23 mm/m.y. and an absence of recently deposited materials (ages of outermost layers are 3-5 Ma). These differences between the characteristics of the coatings for samples from the shallower and deeper parts of the UZ may indicate that the nonwelded tuffs (PTn), located between the welded parts of the Tiva Canyon and Topopah Spring Tuffs, play an important role in moderating UZ flow.

Keywords: Yucca Mountain, uranium-lead dating, opal, chalcedony, paleohydrology, unsaturated zone

1. Introduction

Yucca Mountain, in southwestern Nevada, USA, is being evaluated as a site for the construction of a potential high-level radioactive waste repository (U.S. Department of Energy, 1988). Because ground water is a likely medium for transporting radionuclides from the potential repository to the accessible environment, determining the nature and rate of water movement through the UZ at Yucca Mountain is a critical task for assessing the future performance of the potential nuclear waste repository.

General restriction of minerals to lithophysae floors and fracture footwalls as well as chemical and isotopic (C, O, Sr, U) compositions of calcite and silica indicate that the coatings in fractures and cavities at Yucca Mountain were deposited from water percolating down through the UZ (Paces *et al.*, 2001). Nonetheless, fluid inclusions indicating elevated temperatures of calcite deposition (35 to 85 °C) led some authors (Dublyansky *et al.*, 2001) to attribute these deposits to formation from upwelling hydrothermal waters. Deciphering the history of mineral deposition can provide information on percolation processes for the UZ flow modeling, constrain seepage rates of water percolating into subsurface cavities (Marshall *et al.*, 2000), provide

evidence for the timing of formation of fluid inclusions found in the calcite (Hill and Dyblyansky, 1999; Dublyansky *et al.*, 2001; Whelan *et al.*, 2000; Wilson *et al.*, 2000), and establish the time frame for stable isotope records of the deposits (Paces *et al.*, 2001).

Previous studies using opal as a U-Pb geochronometer demonstrated its potential for dating Miocene and Pliocene geologic events (Ludwig *et al.*, 1980; Zielinski, 1982). Opal and chalcedony from the UZ at Yucca Mountain have large concentrations of U (10^1 to 10^2 μg/g compared to 10^{-3} to 10^{-2} μg/g in pure calcite) along with small concentrations of non-hydrophilic Th and Pb (Paces, Neymark *et al.*, 1998; Paces *et al.*, 2001; Neymark and Paces, 2000; Neymark *et al.*, 2000), making small samples of discreet microstratigraphic layers of silica within coatings of these minerals suitable for U-Pb dating. Previous U-series and U-Pb dating of opal from the outermost surfaces of the mineral coatings (Paces, Neymark *et al.*, 1998 and Paces *et al.*, 2001; Neymark and Paces, 2000; Neymark *et al.*, 2000) determined that the outermost 0.5-2-mm-thick layers of the coatings were formed during the last million years, but silica from interior microstratigraphic layers was not analyzed. This paper reports analyses of U-Th-Pb isotope systems in silica from different interior microstratigraphic layers in the coatings performed to determine U-Pb ages and to test their consistency with internal microstratigraphic relations, to reconstruct the depositional history of the coatings, and to estimate long-term average rates of mineral deposition.

2. Geologic Setting

Yucca Mountain is composed of a 1- to 3-km-thick sequence of felsic volcanic rocks that erupted 12.8 to 12.7 m.y. ago (Sawyer *et al.*, 1994). Cooling joints, shears, faults, and fractures form a network of potential pathways that may facilitate water movement within the otherwise low-permeability welded tuff. The hydrogeology of the site is described in more detail by Stuckless and Dudley (this issue). Because this paper presents data that are directly applicable to

the hydrogeology of the site, hydrogeologic units (Montazer and Wilson, 1984) are used rather than lithostratigraphic units to describe different types of host tuffs from which fracture and cavity coating samples were collected. The moderately to densely welded units within the Tiva Canyon (TCw) and Topopah Spring (TSw) Tuffs have small matrix permeability and large fracture permeability (Montazer and Wilson, 1984). The nonwelded lower part of the Tiva Canyon Tuff, intervening nonwelded tuffs of the Paintbrush Group, and the nonwelded upper part of the Topopah Spring Tuff form the Paintbrush Tuff nonwelded (PTn) hydrogeologic unit, which has large matrix permeability and few fractures (Montazer and Wilson, 1984). Correlations between hydrogeologic and lithostratigraphic units have been described by Buesch *et al.* (1996).

Once the tuffs cooled enough to allow percolation of liquid water, silica (including quartz, chalcedony, and opal) and calcite might have started to precipitate as coatings on a small number of fractures and lithophysal cavities (primary voids formed by volcanic gases during cooling of the tuffs). A general description of the mineral paragenesis of the coatings at Yucca Mountain and evidence of their formation in the hydrologically unsaturated environment are given in Paces *et al.* (2001).

3. Samples

Samples of silica were collected from calcite and silica coatings in fractures and cavities in the Exploratory Studies Facility (ESF) tunnel (Fig. 1a). Distances in the ESF are measured in meters from the north portal of the tunnel. Depths in the ESF are from the three-dimensional integrated site model of Yucca Mountain (W.P. Zelinski and R.W. Clayton, URS Corporation, 1996, written communication). The term silica is used in this paper to denote opal, chalcedony, or quartz; nomenclature of different silica varieties is adopted from Jones and Segnit (1971) and Flörke *et al.* (1982). The term sample is used for individual pieces of calcite and silica coatings

collected in the field and the term subsample is used for silica fractions separated in the laboratory from an individual calcite and silica coating, usually from a distinct layer.

From the 16 calcite and silica coating samples, 85 subsamples of opal, chalcedony, and quartz (along with some adhering calcite) were selected for U-Th-Pb isotope analyses. These samples do not represent all the varieties of calcite and silica deposits observed in the ESF; most were collected from the thickest coatings in lithophysal cavities and fractures so that silica from different microstratigraphic layers could be readily separated. Three samples, HD1838, HD2260, and HD2257 were collected from the TCw above the PTn in the north and south ramps of the ESF from depths of about 50 m below the land surface. Five samples from the TSw in the north and south ramps of the ESF are from intermediate depths (100-200 m), and eight samples from the TSw in the main drift of the ESF are from depths between 200 and 300 m (Fig. 1 b).

For 10 of the mineral coating samples, multiple silica layers from different microstratigraphic positions within each sample were subsampled. The number of silica subsamples for each mineral coating in most cases was limited by the availability of silica layers, especially in those samples consisting mainly of calcite. Multiple chalcedony subsamples were collected from 1- to 2-cm-thick mineral coating samples from fractures (HD2021, HD2029, and HD2257). Two quartz subsamples also were collected from sample HD2021. Multiple opal subsamples were collected from six 9- to 37-mm-thick mineral coatings from lithophysal cavities (samples HD2019, HD2019A, HD2019A1, HD2055, HD2059, HD2074, and HD2357), which contained opal intercalated with calcite at different microstratigraphic levels. One additional opal subsample was collected from a mineral coating HD2054 in a lithophysal cavity. In addition, four silica subsamples (HD2093Pb1, HD2238Pb1, HD2247APb1, and HD2260Pb1) were collected from layers overlying calcite that has low $\delta^{18}O$ values of ~ 3 to 10 relative to SMOW (Paces *et al.*, 2001).

4. Methods

4.1. Analytical Techniques

Calcite and silica coating samples were subsampled at the U.S. Geological Survey (USGS), Yucca Mountain Project Branch laboratory in Denver. Mineral coatings were sliced parallel to their direction of growth and polished. Initially, relatively large (tens of milligrams) silica subsamples were analyzed, but in the course of this study it was shown that reliable data could be obtained for opal subsamples as small as tenths of a milligram. Silica subsamples from different microstratigraphic layers within individual coatings were separated from surrounding calcite with 0.3- to 0.5-mm-diameter carbide- or diamond-coated dental drill burs. Opal and chalcedony fragments were then pried off with a sharp needle or tweezers. Separation of silica was assisted by short-wavelength ultraviolet light, under which opal and chalcedony fluoresce bright green. For subsamples 2019APb1 and -Pb2, the powder from the separation process also was included. After the U-Pb analyses for these powders indicated large amounts of common Pb, contamination during sampling was suggested and powders were not included for any other subsamples.

U-Th-Pb isotopic systematics were determined for most of the subsamples at the Jack Satterly Geochronology Laboratory, Royal Ontario Museum, Toronto, Canada. All the subsamples were leached mildly with high purity 2N HCl at room temperature in order to remove surface contamination and dissolve adherent calcite. Details of the acid leaching and chemical and isotope analysis techniques are described in Neymark *et al.* (2000). Only leaches from powdered subsamples of HD2019A were analyzed. The Pb and U isotopic data were reduced using the PBDAT program (Ludwig, 1987), which makes corrections for mass-discrimination, procedure blank, spike contribution, and initial common Pb. Total procedure blanks were measured repeatedly during this study (one blank per each 8-10 samples) and averaged 1.5 ± 1.0 (all errors in this paper are 2σ) and 0.1 ± 0.1 picograms for Pb and U, respectively. The isotopic composition of the Pb blank was determined as 17.95 ± 1.53

($^{206}Pb/^{204}Pb$), 15.31 ± 1.05 ($^{207}Pb/^{204}Pb$), and 36.68 ± 2.79 ($^{208}Pb/^{204}Pb$), with a correlation coefficient between $^{207}Pb/^{204}Pb$ and $^{206}Pb/^{204}Pb$ of 0.8.

U-Pb data for sample HD2074 were obtained at the USGS Yucca Mountain Project Branch laboratory in Denver. The opal subsamples were spiked with a ^{233}U-^{236}U-^{229}Th-^{205}Pb mixed tracer and digested in concentrated HF. The Pb fraction (about 80% of the total dissolved material) and U-Th fraction were loaded on two separate Re filaments without chemical separation. Lead aliquots were loaded with a mixture of H_3PO_4 with colloidal silicic acid (Gerstenberger and Haase, 1997); U and Th aliquots were loaded with graphite suspension. A Finnigan MAT 262 thermal-ionization mass spectrometer equipped with an ion counting system was used for isotopic analyses. Although U can be measured from silica gel loads, the ionization efficiency achieved with the graphite technique is about 100 times greater, which is important for precise measurement of ^{234}U. This "no-chemical-separation" technique gives stable ion beams of Pb for opal subsamples weighing less than 0.2 mg. Total procedure blanks in the Denver laboratory were measured 3 times during this study and averaged 2.5 ± 1, 1.8 ± 0.5, and 10 ± 5 picograms for Pb, U, and Th, respectively. Isotopic composition of lead in the blank was determined as 18.92 ± 1.34 ($^{206}Pb/^{204}Pb$), 15.64 ± 0.82 ($^{207}Pb/^{204}Pb$), and 38.60 ± 1.60 ($^{208}Pb/^{204}Pb$), with a correlation coefficient between $^{207}Pb/^{204}Pb$ and $^{206}Pb/^{204}Pb$ of 0.85.

The thermal ionization mass-spectrometric (TIMS) U-series analytical techniques used for this study in both the Denver and Toronto laboratories have been described in detail elsewhere (Neymark and Paces, 2000; Neymark *et al.*, 2000; Paces *et al.*, 2001). Multiple TIMS analyses in both laboratories of a solution of ~70 Ma uranium ore, which is supposed to be in secular radioactive equilibrium (Ludwig *et al.*, 1985), have calculated [$^{234}U/^{238}U$] and [$^{230}Th/^{238}U$] activity ratios that are within analytical error of unity. Throughout this paper isotopic ratios in square brackets denote activity ratios.

Correction for the presence of common Pb is particularly critical for U-Pb dating of young materials with low concentrations of radiogenic Pb. Common Pb isotope compositions used to correct data presented here are the mean values of previously determined Pb isotope compositions for 7 samples of Yucca Mountain filtered water and 22 samples of subsurface calcite with low U/Pb ratios. The resulting composition is 18.83 ± 0.82 for $^{206}Pb/^{204}Pb$, 15.62 ± 0.09 for $^{207}Pb/^{204}Pb$, and 38.78 ± 0.53 for $^{208}Pb/^{204}Pb$ (R. Zartman and L. Kwak, US Geological Survey, 1993, written communication; unpublished data of the authors). Conventional $^{206}Pb^*/^{238}U$ and $^{207}Pb^*/^{235}U$ (asterisks denote calculated radiogenic Pb after subtraction of the common-Pb component) ages were calculated using the ISOPLOT program (Ludwig, 1997). Decay constants (λ in y^{-1}) used in the calculations are: $\lambda^{238}U=1.55125\cdot10^{-10}$, $\lambda^{235}U=9.8485\cdot10^{-10}$ (Jaffey *et al.*, 1971), $\lambda^{234}U=2.835\cdot10^{-6}$ (DeBievre *et al.*, 1971; Lounsbury and Dunham, 1971), $\lambda^{230}Th=9.1952\cdot10^{-6}$ (Meadows *et al.*, 1980), $\lambda^{226}Ra=4.332\cdot10^{-4}$, $\lambda^{210}Pb=3.151\cdot10^{-2}$, $\lambda^{231}Pa=2.133\cdot10^{-5}$, $\lambda^{227}Ac=3.151\cdot10^{-2}$ (Browne and Firestone, 1986).

4.2. Principles of U-Pb dating for systems in radioactive disequilibrium

The conventional method of calculating U-Pb isotope ages from common Pb-corrected $^{206}Pb^*/^{238}U$ and $^{207}Pb^*/^{235}U$ ratios (Faure, 1986) assumes an initial state of secular equilibrium, that is, activities of all intermediate daughter isotopes were equal to the activity of the parent at the time of mineral formation. Previous U-series studies of Yucca Mountain opals from the outermost surfaces of calcite and silica coatings showed large excesses of ^{234}U and an absence of initial ^{230}Th (Paces, Neymark *et al.*, 1998; Paces *et al.*, 2001; Neymark and Paces, 2000; Neymark *et al.*, 2000). Therefore, more general forms of the age equations for a closed system were used (Bateman, 1910; Catchen, 1984) that are applicable to systems older than 1000 years (that is, only daughter isotopes with half-lives greater than 1 year are considered). These equations take into account initial disequilibrium of ^{234}U and assume negligible initial ^{231}Pa,

^{227}Ac, ^{230}Th, ^{226}Ra, and ^{210}Pb (Ludwig, 1977). The assumed absence of these isotopes in minerals precipitated from oxidizing aqueous solutions is reasonable because of their low solubilities resulting in short residence times in ground water (Gascoyne, 1992; Murphy and Shock, 1999).

The isotopic ratios ^{206}Pb*/^{238}U and ^{207}Pb*/^{235}U correspond to two different radioactive decay systems, allowing calculation of two independent apparent ages. Agreement of these ages proves that the mineral remained closed to migration of U and its daughter isotopes as long as they were in secular equilibrium at the time of mineral formation, or the excess or deficiency of radiogenic Pb due to initial disequilibrium is negligible compared to the total amount of radiogenic Pb formed from ^{238}U and ^{235}U. However, for systems with substantial initial excess of ^{234}U, the age calculation from ^{206}Pb*/^{238}U requires that the initial ^{234}U/^{238}U must be known. Previous U-series data for opal and calcite from the ESF indicate a range of initial [^{234}U/^{238}U] from 2 to 10 (Paces, Neymark *et al.*, 1998; Paces *et al.*, 2001; Neymark and Paces, 2000). Growth of radiogenic Pb from variable excesses of ^{234}U is described by a family of concordia curves for different initial ^{234}U/^{238}U, three of which are shown in Fig. 2. The shape of the concordia curves reflects the rapid growth of radiogenic ^{206}Pb* from the excess ^{234}U during the first 1 m.y. after mineral deposition. When ^{234}U reaches radioactive equilibrium with ^{238}U, the curves become parallel. In contrast, ^{207}Pb*/^{235}U ages are independent of the variations in initial ^{234}U/^{238}U.

The ^{235}U-^{207}Pb decay chain contains no daughter uranium isotopes or other water-soluble long-lived isotopes. Protactinium-231 (^{231}Pa) is the only intermediate nuclide in the ^{235}U decay chain with a half-life long enough to be of geologic interest. In aqueous solutions ^{231}Pa is rapidly removed from water because of its tendency, like Th, to hydrolyze and adsorb on sinking particles (Gascoyne, 1992). It occurs in nature in +4 and +5 oxidation states (Murphy and Shock, 1999), both of which form in water poorly soluble chemical compounds. At Yucca Mountain, initial disequilibrium in the ^{235}U decay chain may be caused by a lack of poorly soluble daughter isotopes ^{231}Pa and shorter-lived ^{227}Ac in the water that precipitated silica. Disequilibrium

$^{207}Pb^*/^{235}U$ ages are about 50 k.y. older than conventional $^{207}Pb^*/^{235}U$ ages because during a given time interval slightly less radiogenic $^{207}Pb^*$ is produced with no initial ^{231}Pa and ^{227}Ac present. Although higher affinity of biogenic opal for adsorption of ^{231}Pa relative to ^{230}Th was suggested in oceans (Walter *et al.*, 1997 and references therein), it is highly unlikely that the Yucca Mountain silica that has very low Th/U ratios and large U concentrations (Neymark and Paces, 2000; Neymark *et al.*, 2000; Paces *et al.*, 2001) contained appreciable initial excesses of ^{231}Pa and ^{227}Ac relative to ^{235}U. Therefore, it is assumed in this paper that initial [$^{231}Pa/^{235}U$] and [$^{227}Ac/^{235}U$] could have ranged from 0 to 1 and that 50 k.y. is the maximum bias in $^{207}Pb^*/^{235}U$ ages of Yucca Mountain silica caused by the initial radioactive disequilibrium.

5. Results

5.1. U, Th, and Pb concentrations and Pb isotope compositions

The three silica phases in the Yucca Mountain subsamples have U concentrations that vary by more than four orders of magnitude and generally small Th and Pb concentrations (Table 1). Two quartz subsamples (HD2021Pb1-b1 and -c1) have small U concentrations of about 0.05 ppm. Chalcedony subsamples have intermediate U concentrations typically between 7.11 and 13.6 ppm. Opal has U concentrations typically between 20 and 300 ppm, which are similar to the values reported previously for opal from Yucca Mountain (Paces, Neymark *et al.*, 1998; Neymark *et al.*, 2000; Neymark and Paces, 2000; Paces *et al.*, 2001). Concentrations of Th (0.106 to 299 ppb, Table 1) are small in all these phases, thus resulting in extremely low Th/U in the Yucca Mountain silica subsamples.

Concentrations of Pb varied from 6 to 387 ppb (Table 1), except for two opal subsamples HD2019APb2 and HD2093Pb1 with much larger Pb concentrations (3136 and 1004 ppb, Table 1). Lead isotope compositions in most subsamples have blank-corrected $^{206}Pb/^{204}Pb$ ratios >50, up to 53,806 (Table 1). Measured $^{208}Pb/^{204}Pb$ ratios in most subsamples typically were non-

radiogenic, consistent with the very low Th concentrations and Th/Pb in the Yucca Mountain silica coatings. Although subsamples with small common Pb contents have large errors for blank-corrected $^{206}Pb/^{204}Pb$, $^{207}Pb/^{204}Pb$, and $^{208}Pb/^{204}Pb$ ratios, errors for radiogenic Pb concentrations ($^{206}Pb^*$ and $^{207}Pb^*$) and for $^{206}Pb^*/^{238}U$ and $^{207}Pb^*/^{235}U$ are small.

5.2. U-Pb ages

The $^{206}Pb^*/^{238}U$ and $^{207}Pb^*/^{235}U$ values for 75 silica subsamples from the ESF mineral coatings (Table 2) are plotted on a concordia diagram in Fig. 2. The isotope ratios for most of the opal subsamples plot above the conventional concordia curve (initial $[^{234}U/^{238}U]$ U_i=1), and below the concordia curve for U_i =8 (Fig. 2). Conventional $^{206}Pb^*/^{238}U$ ages for all silica phases range from 1.239 ± 0.070 to 85.5 ± 1.3 Ma (Table 2). Calculated $^{207}Pb^*/^{206}Pb^*$ ages assuming initial equilibrium are negative in many of the silica subsamples (Table 2). The disequilibrium $^{207}Pb^*/^{235}U$ ages ranged from 0.51 ± 0.17 to 9.8 ± 3.4 Ma, with one value as high as 15.3 ± 3.2 Ma (Table 2). Errors for $^{207}Pb^*/^{235}U$ ages are typically 0.4 to 15% of the reported values, but are larger for chalcedony as a result of the larger common Pb correction and lower radiogenic Pb content. For subsamples HD2019APb1 and –Pb3, $^{207}Pb^*/^{235}U$ ages were determined from the slopes of two-point leach-residue $^{207}Pb/^{204}Pb$ - $^{235}U/^{204}Pb$ isochrons because of the relatively high abundances of common lead in the residues.

About half of each subsample -Pb1, -Pb2, and -Pb3 from sample HD2019A consisted of powdered opal and all three subsamples have low measured $^{206}Pb/^{204}Pb$ ratios and large $^{207}Pb^*/^{235}U$ age errors, indicating the likelihood of contamination by common Pb from the metal drill bur used to obtain the subsample. An age for subsample –Pb2 could not be determined because of very small $^{206}Pb/^{204}Pb$ (Table 1). To improve the precision of the age determinations, subsamples -Pb1, -Pb2, and -Pb3 in HD2019A1 were collected from the same microstratigraphic opal layers as those sampled in HD2019A (Fig. 3). These subsamples have larger measured

$^{206}Pb/^{204}Pb$ (Table 1) and much more precise ages (Table 2), within error limits of ages from corresponding opal layers in HD2019A. The ages range from 1.19 ± 0.06 to 7.67 ± 0.25 Ma and all are in agreement with the microstratigraphy of the coating, with oldest ages at the base of the coating (Fig. 4a).

Three opal layers from sample HD2019 have $^{207}Pb^*/^{235}U$ ages from 4.33 ± 0.09 to 9.35 ± 0.25 Ma (Table 2), in agreement with the microstratigraphy of the coating (Fig. 4a). Opal from the outermost surface of this sample was dated previously (Paces *et al.*, 2001) and yielded the $^{230}Th/U$ age of 0.094±0.002 Ma. Three opal layers in sample HD2055 have ages from 0.17 ± 0.03 to 5.00 ± 0.07 Ma (Table 2 and Neymark *et al.*, 2000), which are consistent with the microstratigraphy (Fig. 4b). Three different opal layers in sample HD2059 have ages from 0.34 ± 0.04 to 5.27 ± 0.02 Ma (Table 2 and Neymark *et al.*, 2000), which also are consistent with the microstratigraphy (Fig. 4c). Two subsamples –Pb1-1 and –Pb1-2 from the same innermost opal layer in HD2059, have only slightly different ages of 5.27 ± 0.02 and 5.11 ± 0.09 Ma (Table 2), further supporting the validity of the obtained age.

Of 14 subsamples collected from different microstratigraphic levels in sample HD2074, only 6 from the inner portion of the crust and 1 from the outermost surface were analyzed for both Pb and U and have age results (Tables 1 and 2). The $^{207}Pb^*/^{235}U$ ages ranged from 0.51 ± 0.17 to 8.0 ± 3.5 Ma. Most of the $^{207}Pb^*/^{235}U$ ages for sample HD2074 are in general agreement with the microstratigraphy (Fig. 4d). However, subsamples -UPb4-1, -UPb5, -UPb7, and -UPb8, representing a 7.6-mm-thick calcite and opal layer (which constitutes more than 20% of the total coating thickness), have ages that overlap within error limits. Subsamples -UPb7 and -UPb8 are from the same V-shaped opal layer coating the paleosurface of a calcite crystal, even though they are from different depths within the coating. The age/depth relations among these four subsamples probably are more a result of complex non-horizontal growth layers than rapid deposition of this part of the coating.

Abundant opal layers within the 1.8-cm-thick coating sample HD2357 allowed analysis of 15 opal subsamples from different microstratigraphic layers (Fig. 5). In order to refine the spatial resolution of dating, subsamples as small as 0.015 mg were analyzed (Table 1). The $^{207}Pb^*/^{235}U$ ages ranged from 1.65 ± 0.34 to 6.17 ± 0.45 Ma (Table 2) and are in general agreement with the microstratigraphy of the coating (Fig. 5), although several deviations were observed. For example, microstratigraphically youngest subsamples -Pb1 and -Pb2, collected from the outermost surface of the coating, have ages of 2.48 ± 0.02 and 2.66 ± 0.03 Ma, respectively, whereas subsamples -Pb7-1 and Pb7-2, collected about 0.5 cm below the surface of the coating, have younger ages of 1.87 ± 0.10 and 1.65 ± 0.34 Ma. Unlike most samples from lithophysal cavities, this coating has a relatively old $^{207}Pb^*/^{235}U$ age for the outermost surface. Also the age for -Pb3 (5.04 ± 0.03 Ma) was older than ages for several microstratigraphically deeper subsamples (Table 2, Fig. 5). The age deviations in this coating may reflect a complex depositional history, open system behavior, replacement of previously formed calcite and opal by younger silica, and (or) rapid deposition of at least the inner two-thirds of this coating.

Sample HD1838, mainly consisting of opal with lesser intercalated calcite, allowed analysis of 10 silica subsamples, which, except for subsamples –f and –g, have microstratigraphically consistent $^{207}Pb^*/^{235}U$ ages from 6.42 ± 0.60 to 3.13 ± 0.05 Ma (Table 2, Fig. 6a). Subsamples –f and –g have low measured $^{207}Pb/^{204}Pb$ and very low U contents of 2.63 and 1.47 ppm as compared to 5.98 to 63.1 ppm for other subsamples from this coating sample (Table 1). Uranium loss is suggested for these subsamples and their ages, which are inconsistent with the microstratigraphy, are considered unreliable and are not shown in the figure.

In contrast to data from most coatings, youngest $^{207}Pb^*/^{235}U$ ages were obtained for deeper subsamples in HD2257 (Fig. 6b), in sharp disagreement with observed microstratigraphy. The $^{207}Pb^*/^{235}U$ ages for the inner layers of sample HD2257 ranged from 8.8 5± 0.40 to 7.04 ± 0.91 Ma. Also, three optically different silica varieties analyzed separately for subsample -Pb1 from

the outermost surface of the coating have inconsistent ages ranging from 8.98 ± 0.67 to 5.67 ± 0.15 Ma, significantly older than outermost surface ages for most samples. The youngest age was obtained for the subsample with a much larger U concentration (56.9 ppm) than the concentrations of about 3 to 17 ppm in the other subsamples of HD2257 (Tables 1 and 2, Fig. 6b). In addition, there is a rough negative correlation between the U concentration and the calculated apparent age, with subsample HD2257Pb7, which has the lowest concentration of 2.86 ppm U (Table 1), yielding a relatively imprecise $^{207}Pb^*/^{235}U$ age of 15.3 ± 3.2 Ma. This unreasonably old age is explained most plausibly by open-system conditions, where preferential U loss results in apparent U-Pb ages that are concordant within error limits (Table 2), but are too old. However, uranium loss cannot explain the old ages of most of the other subsamples from HD2257, because U-Pb data plot below the equilibrium concordia diagram (Fig. 7a), which requires preferential loss of uranium daughter decay products. Potential reasons for concordant ages that are too old geologically and data plotting below the equilibrium concordia for the ESF silica are discussed below in section 6.2.

Six chalcedony subsamples from different microstratigraphic positions within sample HD2021, a coating about 1.3 cm thick, have overlapping (within error limits) $^{207}Pb^*/^{235}U$ ages of 9.35 ± 0.41 to 9.68 ± 0.77 Ma (Table 2 and Fig. 8). Unlike data from most Yucca Mountain fracture opals, these chalcedony data plot below the equilibrium concordia diagram (Fig. 7b) displaying "normal" age discordance where $^{207}Pb^*/^{235}U$ age > $^{206}Pb^*/^{238}U$ age. Similar discordant data were obtained for two chalcedony subsamples from sample HD2029 (Table 2). No reasonable age information was obtained for two quartz subsamples from this coating (–Pb1-b1 and –Pb1-c1) because the U concentrations and $^{238}U/^{204}Pb$ were too small (Table 1).

5.3. Measured $^{234}U/^{238}U$, $^{230}Th/^{238}U$ and $^{230}Th/U$ ages

Most measured [$^{234}U/^{238}U$] and [$^{230}Th/^{238}U$] were within analytical error of unity (Table 1). Subsamples HD2019A1Pb4, HD2074UPb11 and -11a, and HD2055Pb2, collected from microstratigraphic positions near the outermost surface of the coatings, have [$^{234}U/^{238}U$] greater than unity (Table 1). Subsamples from HD1838, HD2257, HD2357, and subsamples HD2074UPb1 and HD2055Pb3-2, both from deeper layers, have measured [$^{234}U/^{238}U$] and [$^{230}Th/^{238}U$] that deviated from unity beyond the error limits.

U-series ages were calculated for two subsamples where both [$^{230}Th/^{238}U$] and [$^{234}U/^{238}U$] appreciably exceeded unity (Table 1). Subsample HD2074UPb11a, collected from the outermost surface of the coating (Fig. 4d), has a $^{230}Th/U$ age of 0.242 ± 0.024 Ma (calculated from U-series data in Table 1), which is appreciably younger than the $^{207}Pb^*/^{235}U$ age of this subsample (0.51 ± 0.17 Ma, Table 2). Discordant $^{230}Th/U$ (292 ± 17 ka, calculated from U-series data in Table 1) and $^{207}Pb^*/^{235}U$ (1.19 ± 0.06 Ma, Table 2) ages also were obtained for subsample HD2019A1Pb4, collected from an inner layer of the coating. Probable reasons for the age discordance and the radioactive disequilibrium in old samples will be discussed in the following section.

6. Discussion

6.1. Geological meaning and reliability of U-Pb ages of silica mineral coatings

U-Pb dating of silica in mineral coatings determines the time when migration of uranium and its daughter products ceased and (or) when their diffusion became much slower relative to the rate of radioactive decay. If amorphous opal-A forms from maturing silica gel precipitated from water (Ludwig *et al.* 1980; Zielinski, 1982), its U-Pb age would reflect the time when the water redistribution and migration of dissolved ions terminated within the precipitating solid phase. This is probably very close to the time of the silica gel deposition, assuming closed system

behavior from that time until the present. However, subsequent crystallographic ordering and transformations like opal-A → opal-CT → chalcedony complicate the exact meaning of U-Pb ages. These transformations may be caused by changes in thermal conditions and aging of opal (Kano, 1983; Thiry and Millot, 1987; Herdianita *et al.*, 2000), although chalcedony also may precipitate directly from solutions (Heaney, 1993). If the observed decrease in U concentration from opal to chalcedony in the fracture silica at Yucca Mountain is caused by the U loss during these mineralogical transformations, the meaning of U-Pb ages will depend on the duration and rate of these ordering processes. If the different silica phases formed directly from the UZ water, or if these silica transformations occurred rapidly after deposition, the U-Pb age would reflect the age of deposition. For slow transformations, the U-Pb ages would reflect an average age of the continuous processes. Age interpretations may be further complicated because it is not clear whether silica transformations fractionate U and Pb.

Even in the case of closed-system behavior with no mineral transformations, the U-Pb ages for Yucca Mountain UZ silica may represent average ages of mineral deposition. Slow rates of growth in outermost opal layers of these coatings and limited spatial resolution of sampling result in analysis of complex multi-age materials even for subsample sizes less than 1 mg (Paces, Neymark *et al.*, 1998; Paces *et al.*, 2001; Neymark and Paces, 2000; Neymark *et al.*, 2000). Therefore, it is likely that U-series and U-Pb ages are average ages for silica deposition within the sampled microstratigraphic intervals.

Despite the complications related to initial disequilibrium and other complexities in interpretation of U-Pb data discussed below, several lines of evidence indicate that the $^{207}Pb^*/^{235}U$ ages represent reliable ages of the mineral deposition in most cases. First, previous acid leaching experiments of calcite and opal mixtures (Neymark and Paces, 2000) and pure opal (Neymark *et al.*, 2000) showed that U-Th-Pb isotope systems in opals were considerably resistant to short-term interactions with reactive media (HCl and acetic acid). Therefore opal, poorly

soluble at pH < 9 (Dove and Rimstidt, 1994), likely preserves its U-Pb isotope signatures from the time of mineral deposition even though it may be exposed to near neutral water in the UZ (pH of about 7-8, Meijer, 1990) under low-temperature conditions after deposition. Second, opals younger than about 2 Ma with directly measured excesses of ^{234}U have ^{206}Pb-^{234}U-^{238}U ages that are concordant with $^{207}Pb^*/^{235}U$ ages in most cases (Neymark *et al.*, 2000). There is no reason to expect that older opals would behave in a dramatically different way than opals younger than 2 Ma from the same fracture and cavity coatings. Third, most opals collected at different depths within individual crusts in the deeper UZ have $^{207}Pb^*/^{235}U$ ages that not only agree with the microstratigraphic positions, but also result in uniform long-term average rates of deposition within and between the coatings (see section 6.7). Finally, with only one exception, all opal and chalcedony $^{207}Pb^*/^{235}U$ ages (Table 2) are within error limits or younger than the age of the host tuffs of 12.7 to 12.8 Ma (Sawyer *et al.*, 1994).

6.2. Discordance of U-Pb ages

A common measure for the reliability of U-Pb ages is the degree of concordance between ages calculated from $^{207}Pb^*/^{235}U$ and $^{206}Pb^*/^{238}U$ using conventional equations of radioactive decay (Faure, 1986). Equal ages prove that the mineral remained closed to migration of U and its daughter isotopes. This approach is valid as long as uranium and its decay products are in secular equilibrium at the time of the mineral formation. For minerals of Miocene and younger age the criterion of concordance of $^{207}Pb^*/^{235}U$ and $^{206}Pb^*/^{238}U$ ages as an indication of closed system behavior may not be valid. Modern U loss or gain, Pb loss, and two-component mixing of younger and older opals would result in data points plotting along a straight line intersecting the origin of coordinates. Because of the very small curvature of conventional concordia in the 0 to 10 m.y. age range (Fig. 2), the concordia would coincide with this straight line and no age discordance could be detected even for high-precision data. Additionally, the age concordance

criterion is not applicable to U-Pb systems with severe initial radioactive disequilibrium, such as is likely true for Yucca Mountain silica, where reverse discordance of conventional $^{207}Pb^*/^{235}U$ and $^{206}Pb^*/^{238}U$ ages is not necessarily indicative of open system behavior. Conventional U-Pb ages in the Yucca Mountain silica have both normal ($^{207}Pb^*/^{235}U$ age > $^{206}Pb^*/^{238}U$ age) and reverse ($^{207}Pb^*/^{235}U$ age< $^{206}Pb^*/^{238}U$ age) discordance (Table 2, Fig. 2).

Normal discordance of U-Pb data for chalcedony subsamples from HD2021, HD2257 (except -Pb7), and HD2029 (Table 2 and Fig. 7) is indicative of the preferential continuous loss of U-decay products. Episodic losses would not create measurable age discordance (see above). An initial excess of ^{231}Pa, that also could cause the observed discordance pattern, is unlikely, as discussed in section 4.2. The data points in Fig. 7a and b follow patterns for U-Pb systems with continuous leakage of both radiogenic Pb and radioactive daughters of ^{238}U such as Rn (Ludwig *et al.*, 1984). Additional evidence for the potential Rn leakage from the Yucca Mountain secondary silica is provided by the absence of any measurable ^4He in sample HD2021 (K. Farley, Caltech, 2000, written communication). The discordia paths (curved lines) that best fit the data were calculated using the ISOPLOT program (Ludwig, 1997) for the case of simultaneous Rn and Pb loss when the ratio of their diffusion coefficients $D_{Rn}/D_{Pb} = 5 \cdot 10^8$. Because initial $[^{234}U/^{238}U]$ (U_i) for these samples are not known, the ages can be constrained by the intersections of the diffusion discordia lines with two concordia curves corresponding to $U_i = 1$ (equilibrium) and $U_i = 10$ (disequilibrium) (Fig. 7 a and b). These U_i values cover the range determined from young (<100 ka) UZ fracture and cavity minerals at Yucca Mountain (Paces, Neymark *et al.*, 1998; Paces *et al.*, 2001). The discordia lines intersect concordia curves at ages of about 9.0 and 10.4 Ma for sample HD2257 and about 9.8 and 11.4 Ma for sample HD2021. These discordance patterns and the similarity of $^{207}Pb^*/^{235}U$ ages for multiple subsamples collected from different microstratigraphic positions in both samples (Fig. 6b and 8) may indicate resetting of U-Pb systems in these subsamples rather than true ages of silica deposition. Therefore, the $^{207}Pb^*/^{235}U$

ages for these samples presented in Table 2 and Figures 6b, 8, 9, and 11a would be minimum ages of these minerals.

The reverse discordance of conventional U-Pb ages observed for most opal samples does not require open system behavior, but more likely is caused by large and variable [$^{234}U/^{238}U$] (2 to 8, Fig. 2) ratios in waters from which these opals precipitated. Excess ^{206}Pb in reversely discordant analyses is consistent with the large [$^{234}U/^{238}U$] observed in modern UZ water (Paces, Ludwig *et al.*, 1998) and large U_i values reported for Yucca Mountain UZ minerals of Pleistocene age (Paces, Neymark *et al.*, 1998; Paces *et al.*, 2001; Neymark and Paces, 2000).

6.3. $^{207}Pb^*/^{235}U$ ages and radioactive disequilibrium

Additional information on the closed or open system behavior of U and its decay products was obtained by assessing their consistency with measured $^{234}U/^{238}U$ for most subsamples and by comparing $^{207}Pb^*/^{235}U$ ages with $^{230}Th/U$ ages for two subsamples. Most measured [$^{234}U/^{238}U$] and [$^{230}Th/^{238}U$] were within analytical error of unity (Table 1), consistent with the old (> 1.0 Ma) U-Pb ages of the subsamples and indicating that these silica subsamples remained closed relative to U and Th mobility during the past several hundred thousand years. Subsamples with measured [$^{234}U/^{238}U$] that deviated from unity beyond the error limits (Table 1) may indicate closed or open system behavior, depending on the age. Subsamples HD2019A1Pb4, HD2074UPb11 and -11a, and HD2055Pb2, collected from microstratigraphic positions near the outermost surface of the coatings, have [$^{234}U/^{238}U$] greater than unity (Table 1), consistent with their young relative ages and the elevated [$^{234}U/^{238}U$] in water percolating through UZ fractures. For hypothetical opals precipitated 1 and 2 m.y. ago from water with [$^{234}U/^{238}U$] = 8, present-day [$^{234}U/^{238}U$] values would be 1.41 and 1.02, respectively. Measured [$^{234}U/^{238}U$] slightly greater than unity in subsamples with $^{207}Pb^*/^{235}U$ ages younger than about 2 Ma (Tables 1 and 2) may be explained as the remnants of excess ^{234}U present at the time of mineral deposition. Some

subsamples from HD2357 and subsample HD2074UPb1, regardless of their old $^{207}Pb^*/^{235}U$ ages, have measured [$^{234}U/^{238}U$] and [$^{230}Th/^{238}U$] greater than unity beyond the error limits. Radioactive disequilibrium in these samples indicates U exchange between old silica and young fracture water and (or) small admixtures of younger opal in these subsamples. Values of [$^{234}U/^{238}U$] between 0.95 and 1 for some subsamples from HD1838, HD2257 and HD2055 (Table 1) likely are caused by Quaternary leaching of U with preferential loss of ^{234}U, probably due to the α-recoil (Kigoshi, 1971) and Szillard-Chalmers (1934) effects. A similar degree of ^{234}U deficit was observed in samples of the tuffs in the ESF (Gascoyne *et al.*, this issue).

The U-series ages calculated for two subsamples where both [$^{234}U/^{238}U$] and [$^{230}Th/^{238}U$] appreciably exceeded unity are discordant with the $^{207}Pb^*/^{235}U$ ages for the subsamples. The age discordance between the $^{207}Pb^*/^{235}U$ (0.51 ± 0.17 Ma, Table 2) and $^{230}Th/U$ (0.242 ± 0.024 Ma, calculated from U-series data in Table 1) ages in the outermost surface subsample HD2074UPb11a (Fig. 4d) is consistent with the age discordance between U-Pb and U-series data previously observed in silica from outermost surfaces of coatings at Yucca Mountain (Neymark *et al.*, 2000). This type of discordance does not require an open system behavior of U and (or) its daughters. Additions of thin, younger layers to a slowly growing opal surface result in a non-linear decrease in the $^{230}Th/U$ age relative to the true average age when multi-aged materials are mixed in a subsample (Neymark and Paces, 2000). The discordance between the systems is the result of the much longer half-life of ^{235}U than that for ^{234}U and ^{230}Th as discussed by Neymark *et al.* (2000). In HD2074UPb11a, the $^{207}Pb^*/^{235}U$ age of 0.51 ± 0.17 Ma is a good estimate of the average age, meaning that the material analyzed probably represents over a million years of opal deposition.

The discordance between the $^{207}Pb^*/^{235}U$ (1.19 ± 0.06 Ma, Table 2) and $^{230}Th/U$ (0.292 ± 0.017 Ma, calculated from U-series data in Table 1) ages for subsample HD2019A1Pb4 also could be interpreted as possible mixing of older and younger opal, assuming that mineral

coatings are growing by additions of new materials to outer surfaces of coatings. However, this subsample was collected from an interior opal layer (Fig. 3) so recent growth on outer surfaces (Neymark *et al.*, 2000) cannot explain the observed age discordance. For two-component mixing of older (in secular equilibrium with regard to ^{234}U) and younger (not in secular equilibrium) opal components, the $^{207}Pb^*/^{235}U$ age of 1.19 ± 0.06 Ma would represent a minimum age of deposition for the older opal component. A similar interpretation may explain the $[^{234}U/^{238}U]$ of 1.506 ± 0.035 (Table 1) for subsample HD2074UPb1, collected from the basal part of the coating (Fig. 4d). Because a younger opal component may be present, the $^{207}Pb^*/^{235}U$ age of 8.0 ± 3.5 Ma for subsample HD2074UPb1 should be considered a minimum depositional age. The large $[^{234}U/^{238}U]$ for HD2074UPb1 may indicate that basal portions of some calcite and silica crusts with large porosity (Paces *et al.*, 2001) contain evidence for post-depositional interactions with fracture water that resulted in modification of U-Th-Pb isotope systems.

6.4. U-Pb ages for subsamples with the same geological age

U-Pb ages for petrographically distinct silica from the same microstratigraphic layer (presumably with the same age of deposition) were obtained for seven subsamples (Table 2). Three opal splits of subsample HD2019A1Pb3 with different degrees of transparency have almost identical $^{207}Pb^*/^{235}U$ ages of 3.92 ± 0.03, 3.99 ± 0.04, and 3.90 ± 0.03 Ma (Fig. 3 and Table 2). The reproducibility of ages for these three splits from the same layer indicates reliability of the ages and the method. Similarly, ages overlapping within the error limits were obtained for opal splits of subsamples HD2059Pb1, HD2357Pb7, and HD2357Pb13 (Table 2 and Fig. 5). In contrast, three multi-milligram splits from the same layer in HD2019Pb3, containing a variety of silica textures, have inconsistent $^{207}Pb^*/^{235}U$ ages of 5.22 ± 0.06, 6.97 ± 0.12, and 9.35 ± 0.25 Ma (Table 2 and Fig. 4a). Subsample -Pb3-2 with the oldest $^{207}Pb^*/^{235}U$ age has the smallest U concentration (6.56 ppm versus 44.0 and 194 ppm in the two other subsamples, Table

1), and consisted of abundant quartz crystals and optically heterogeneous opal. The large, multi-milligram sizes of the subsamples (Table 1) increase the probability of analyzing mixtures of multi-aged materials, and the $^{207}Pb^*/^{235}U$ ages of 9.35 ± 0.25 for –Pb3-1, 6.97 ± 0.12 for –Pb3-1 and 5.22 ± 0.06 Ma for -Pb3-3 are interpreted as real age heterogeneity within this silica layer. Analyzing one opal and two chalcedony subsamples from HD2257Pb1 (Table 2 and Fig. 6b) revealed similar age heterogeneity. Different $^{207}Pb/^{235}U$ ages were obtained for subsamples -Pb3-1 (5.00 ± 0.07 Ma) and -Pb3-2 (3.31 ± 0.05 Ma) (Table 2), collected from the same innermost opal layer in sample HD2055 (Fig. 4b). The disagreement between these two ages may indicate open system behavior, or overgrowth or replacement of old opal with younger opal.

At the current level of understanding of U-Pb systems in secondary silica at Yucca Mountain it is difficult to develop strong and clear universal criteria that would allow distinguishing open U-Pb systems from mixed closed systems. Age results for multiple subsamples from the same microstratigraphic layer emphasize the need for better spatial resolution of microsampling and for careful separation of silica varieties for U-Pb dating. Detailed XRD analyses of the degree of ordering in the silica minerals along with ages of different varieties from the same microstratigraphic layer might provide a better understanding of the behavior of U-Pb systems in these silica deposits.

6.5. Initial $^{234}U/^{238}U$ activity ratios calculated from U-Pb data.

The $^{207}Pb^*/^{235}U$ disequilibrium ages also were used to calculate initial $[^{234}U/^{238}U]$ (U_i) from the measured $^{206}Pb^*/^{238}U$ (Table 2), assuming closed-system behavior. Isotopic compositions plotting above the conventional concordia curve (Fig. 2) are assumed to represent closed system behavior such that calculated U_i values greater than 1 reflect elevated $[^{234}U/^{238}U]$ in water from which silica precipitated in fractures and cavities. However, the data for chalcedony with normal age discordance plotting below the conventional concordia curve (Fig. 2 and 7) give calculated

apparent U_i values that are less than unity (Table 2), thus clearly indicating that ^{234}U was lost preferentially in these subsamples and U-Pb systems were open.

Most calculated U_i for opals ranged from 1.18 ± 0.10 to 13.6 ± 0.5 (Table 2). This range is slightly larger than the range of $[^{234}U/^{238}U]$ from ~3 to ~8 previously observed in Yucca Mountain waters (Paces, Ludwig *et al.*, 1998). The $U_i < 3$ probably are the result of preferential losses of U decay products. The $U_i > 8$ probably are the result of U loss and (or) initial presence of ^{238}U decay products such as ^{226}Ra.

Differences in calculated U_i values for subsamples HD2055Pb3-1 and -Pb3-2 (Table 2) are likely caused by open system behavior in the U decay chain. Both subsamples were collected from the same opal layer and presumably should have the same U_i and age of deposition. However, their ages also are different well outside error limits (5.00 ± 0.07 and 3.31 ± 0.05 Ma, Table 2). Subsample HD2055Pb3-2, with the younger $^{207}Pb^*/^{235}U$ apparent age, also has a much smaller U_i value of 1.18 ± 0.10 versus a U_i of 7.15 ± 0.15 for subsample -Pb3-1 (Table 2). The latter U_i value is closer to the U_i in the range of 4.5 to 6.0 obtained from U-series data for the outermost opal layers from this same sample (Neymark *et al.*, 2000; Paces *et al.*, 2001). These data indicate that either subsample -Pb3-2 formed more recently from water with $[^{234}U/^{238}U]$ of about 1.2, or its U-Pb system was reset, lost almost all radiogenic Pb, and started to re-accumulate it after much of the original excess ^{234}U decayed in the first 1.7 m.y. A continuous simultaneous loss of Rn and Pb from subsample -Pb3-2 also would result in the younger $^{207}Pb^*/^{235}U$ age and smaller calculated U_i value.

6.6. Distribution of $^{207}Pb^*/^{235}U$ ages in time

Despite the complexities in U-Pb systematics discussed above, the range of calculated $^{207}Pb^*/^{235}U$ ages for chalcedony and opal from 0.51 ± 0.17 to 9.84 ± 0.17 Ma clearly indicates that calcite and silica deposition within Yucca Mountain is a long-term process occurring at least for

the past 10 million years. The data can be used to interpret whether the coatings formed slowly as a result of deposition of numerous very thin layers, or rapidly during a few distinct depositional events. Because most samples are dominantly calcite with thin, intercalated silica layers, silica deposition represents distinct episodes in the formation history of the coatings, but there is no evidence that silica deposition in samples collected in different parts of the UZ at Yucca Mountain occurred during a few distinct time intervals (Table 2; Fig. 9). Although the histogram shows a large frequency of $^{207}Pb^*/^{235}U$ ages <1.5 Ma, most of these analyses were specifically targeted at dating outer surfaces (Neymark *et al.*, 2000) and do not reflect a true increase in silica formation in the relatively recent past. As stated previously in this paper, calculated ages of silica subsamples likely represent average ages of materials deposited over tens or hundreds of thousands of years. For this reason, ages for silica coating samples cannot be correlated readily with relatively rapid geological events such as climatic changes or volcanic eruptions.

The $^{207}Pb^*/^{235}U$ ages for subsamples HD2093Pb1, HD2238Pb1, HD2247APb1, and HD2260Pb1, which were collected from silica layers overlying previously analyzed calcite with $\delta^{18}O_{VSMOW}$ values of about 3 to 10 (Paces *et al.*, 2001), were 3.97, 7.5, 7.91, and 9.7 Ma (Table 2). The low $\delta^{18}O$ values are consistent with formation of calcite at higher temperatures, and these ages restrict the elevated temperatures to the early history of the coatings.

Although no analytically reliable $^{207}Pb^*/^{235}U$ ages older than ~10 Ma were obtained for silica sampled in this study (Table 2, Fig. 9), the presence of calcite underlying the oldest dated silica indicates mineral deposition before this time. For example, in sample HD2029 an 8-mm-thick calcite layer is present below the chalcedony layer with the minimum age of 9.84 ± 0.17 Ma. The same is true for opal subsample HD2093Pb1, which was dated at 9.7 ± 1.5 Ma and was collected above a calcite layer. The absence of $^{207}Pb^*/^{235}U$ ages older than ~10 Ma and the normal discordance of U-Pb ages in oldest chalcedony samples (discussed above in section 6.2) indicate the resetting of U-Pb systems in previously deposited silica as a result of a superimposed

geologic event(s). The possibility of a thermal overprint around 10 Ma is supported by K-Ar ages of illite from drill-core samples of altered tuffs in the saturated zone beneath the northern part of Yucca Mountain that indicate a hydrothermal alteration at 11 to 10 Ma (Bish and Aronson, 1993). Similar K-Ar ages were obtained for hydro-micas from a zeolite-rich zone above the hydrothermally altered tuffs (WoldeGabriel, 1995).

6.7. Long-term average rates of deposition and implications for the site paleohydrology

Long-term average rates of UZ calcite and silica deposition were calculated using $^{207}Pb^*/^{235}U$ ages of silica from different microstratigraphic depths within individual mineral coatings (Table 3). Relative depths of sampled layers (the depth to the middle of the sampled layer divided by the total thickness of the coating) were calculated to compare data for coatings of variable thickness at the same relative scale. A subsample collected from the surface of a coating has a relative depth of 0, and from the bottom a relative depth of 1.

Extremely slow (mm/m.y.) and uniform long-term average rates of mineral deposition in the deeper part of the UZ in TSw lithophysal cavities were first proposed by Neymark *et al.* (1998). This observation was based on ages from five samples (HD2019A and -A1, HD2059, HD2055, and HD2019) where only a few opal layers were dated (Fig. 10a, b, c, and d). Long-term average rates of deposition in TSw lithophysal cavities were more thoroughly investigated in samples HD2357 and HD2074 using more subsampled layers (Fig. 10e and f). These coatings have a greater degree of complexity, but generally the data confirm the previously determined slow growth rate. Long-term average rates of deposition ranged from 1.31 ± 0.44 to 5.1 ± 0.8 mm/m.y. (Fig. 10) for these samples from lithophysal cavity floors in the TSw exposed in the ESF main drift. Depositional rates of about 1 mm/m.y. also have been estimated from conventional and ion microprobe (SHRIMP) U-series dating of outermost opal layers for samples from the deeper part of the UZ at Yucca Mountain (Neymark and Paces, 2000; Paces *et al.* 2000, 2001). In order to

decipher more detailed histories of the mineral deposition, a finer spatial resolution of subsampling than that used during this study is required. . Many coatings consist only of calcite and some have only a few datable intercalated silica layers, thus further limiting detailed geochronological studies.

Mineral coatings from fractures in the TCw in the shallower part of the UZ exhibit a different age/depositional depth relation. The $^{207}Pb^*/^{235}U$ ages of five subsamples collected from a ~1-cm-thick intermediate part of coating HD1838 (Table 3, Fig. 6a) are identical within error limits, thus indicating rapid growth of this portion of the coating. A long-term depositional rate of 17.7 ± 5.7 mm/m.y. (Fig. 11a) was calculated for most of this coating, excluding the lowest part. In addition, young material is absent in the outermost portion of this sample. The discordant U-Pb data obtained for sample HD2257 (Fig. 7a), which also was collected above the PTn, can be interpreted as evidence for similar true depositional ages for innermost and outermost layers and may imply a very rapid formation of this coating (Fig. 11a). Young material also is absent from the outermost surface of the coating, with the youngest age 5.67 ± 0.15 Ma for an opal split of HD2257Pb1 and two older ages for chalcedony splits of the same subsample.

The contrast between age-depositional depth relations for mineral coatings on fractures in the shallower part of the UZ above the PTn unit and mineral coatings in lithophysal cavities in the deeper part of the UZ below the PTn unit is evident from the plots in Fig. 11. The main differences between these two data sets are that the samples of fracture coatings from the shallower part of the UZ indicate: 1) an absence of recently deposited materials (ages of outermost layers are 3-5 Ma), 2) possible open system behavior of U and its daughters, and 3) faster apparent deposition rates. These differences in the characteristics of the deposits from above and below the PTn agree with the conceptual UZ flow model of Yucca Mountain originally proposed by Montazer and Wilson (1984) and may reflect a diverting hydrologic role of the PTn nonwelded tuff and the deeper fracture network, both of which would dampen the

effects of variable infiltration (Paces, Neymark *et al.*, 1998; Paces *et al.*, 2001). Uniform long-term average deposition rates in the mineral coatings from lithophysal cavities in the TSw in the deeper part of the UZ (Fig. 10) imply that the hydrologic system in the deeper part of the UZ remained stable for millions of years in spite of a major shift in climate that resulted in increasing aridity and seasonality in the last several million years (Thompson, 1991).

7. Summary and Conclusions

Reliable geochronological information was obtained by U-Pb dating of 75 Neogene- to Quaternary-age chalcedony and opal subsamples from 16 samples of calcite and silica fracture and lithophysal cavity coatings in Miocene-age tuffs at Yucca Mountain. High concentrations of U (commonly 20 to 300 ppm), low concentrations of common Pb ($^{206}Pb/^{204}Pb$ up to 53,806), and a considerable resistance of the silica to short-term interactions with reactive media with regard to loss of uranium and its daughter decay products make the U-Pb system promising as a potential reliable geochronometer for opal and chalcedony. Less than 5 % of the opal and chalcedony samples are suspect for potential uranium losshave low U contents (< 3 ppm) and unreasonably old U-Pb ages. Relatively low U concentrations and high common Pb in two quartz subsamples did not allow any reasonable age calculations.

Conventional U-Pb ages for the opal subsamples display strong reverse discordance and negative $^{207}Pb^*/^{206}Pb^*$ apparent ages because of excess radiogenic $^{206}Pb^*$, presumably derived from the elevated initial ^{234}U inherited from percolating solutions with large $^{234}U/^{238}U$. The $^{207}Pb^*/^{235}U$ ratios are little affected by deviation from initial secular equilibrium and thus may provide reliable ages of most silica deposits. Subsamples of opal and chalcedony have $^{207}Pb^*/^{235}U$ ages between 0.59 and 9.84 Ma. Younger ages are typical for outer subsamples, whereas the oldest ages of about 10 Ma were obtained for chalcedony from the innermost silica layers. As a result of continuous Rn and Pb loss some chalcedony subsamples from basal

portions of coatings, unlike opal, show normal age discordance of U-Pb data, plotting below the conventional concordia curve. Therefore, these $^{207}Pb^*/^{235}U$ ages are considered to be the minimum age of the mineral deposition. Ages of opals from the intermediate layers are generally consistent with the microstratigraphic positions within individual coatings confirming that the coatings grow from the base to the top. The discordance of ages observed in some cases for multiple subsamples from the same microstratigraphic layer and U-series disequilibrium observed in some subsamples with U-Pb ages older than ~ 2 Ma may indicate an open-system behavior and/or additions of younger materials; this may emphasize the need for better spatial resolution of microsampling and for careful separation of silica varieties for U-Pb dating. ^{234}U and ^{230}Th in most silica layers deeper in the coatings are in secular equilibrium with ^{238}U, which is consistent with their old U-Pb age and closed system behavior during the past 0.5 m.y.

The ages of subsamples from silica layers at different microstratigraphic depths in individual mineral coating samples of lithophysal cavities in the TSw (deeper part of the UZ) indicate that many coatings formed at slow long-term average depositional rates of 1 to 5 mm/m.y. The slow depositional rates and limited sampling resolution result in analyses of mixed multi-age silica subsamples and in calculated ages that are likely to represent average ages of materials deposited over tens or hundreds of thousands of years. These data imply that the deeper parts of the UZ at Yucca Mountain maintained long-term hydrologic stability throughout periods of significant climate variations over the past 10 m.y. U-Pb ages for subsamples of silica from different microstratigraphic depths in individual calcite and silica coating samples collected from fractures in the TCw (shallower part of the UZ) indicate faster depositional rates up to 23 mm/m.y. and the absence of recently deposited materials (ages of outermost layers are 3-5 Ma). These differences between the characteristics of the coatings for samples from the shallower and deeper parts of the UZ probably indicate that the nonwelded tuffs (PTn), located between the welded TCw and TSw, play an important role in moderating UZ flow.

Acknowledgements

The work was done in cooperation with the U.S. Department of Energy under Interagency Agreement No. DE-AI08-97NV12033. B. Podstawskji provided mass-spectrometer maintenance at the Royal Ontario Museum and L. Kwak performed chemical analyses in Denver, for which the authors are greatly appreciative.

References

Bateman, H., 1910. Solution of a system of differential equations occurring in the theory of radio-active transformations. Proc. Cambridge Phil. Soc. 15, 423-427.

Bish, D.L., Aronson, J.L., 1993. Paleogeothermal and paleohydrologic conditions in silicic tuff from Yucca Mountain, Nevada. Clays Clay Miner. 41, 148-161.

Browne, E., Firestone, R., 1986. *Table of radioactive isotopes.* John Wiley & Sons, New York.

Buesch, D.C., Spengler, R.W., Moyer, T.C., Geslin, J.K., 1996. Proposed stratigraphic nomenclature and macroscopic identification of lithostratigraphic units of the Paintbrush Group exposed at Yucca Mountain, Nevada. U.S. Geological Survey Open-File Report 94-469, 45 p.

Catchen, G.L., 1984. Application of the equations of radioactive growth and decay to geochronological models and explicit solution of the equations by Laplace transformations. Isot. Geosci. 2, 181-195.

DeBievre, P., Lauer, K.F., Le Duigou, Y., Moret, H., Muschenborn, G., Spaepen, J., Spernol, A., Vaninbroukx, R., Verdingh, V., 1971. The half-life of U-234. In: Hurrell, M.L. (Ed.), Proc. Int. Conf. Chem. Nucl. Data, Measurement and Applications, Canterbury. Inst. Civil Eng. London, pp. 221-225.

Dove, P.M., Rimstidt, J.D., 1994. Silica-water interactions. In: Heaney, P.J., Prewitt, C.T., Gibbs, G.V. (Eds.), Silica: Physical Behavior, Geochemistry and Materials Applications. Reviews in Mineralogy, vol. 29, Mineralogical Society of America, Washington, DC, p. 259-308.

Dublyansky, Y.V., Ford, D.C., Reutsky, V.N., 2001. Traces of epigenetic hydrothermal activity at Yucca Mountain, Nevada: preliminary data on the fluid inclusion and stable isotope evidence. Chem. Geol. 173, 125-149.

Faure, G., 1986. Principles of isotope geology. John Wiley & Sons, New York, 589 p.

Flörke, O.W., Köhler-Herbertz, B., Langer, K., Tönges, I., 1982. Water in microcrystalline quartz of volcanic origin: Agates. Contrib. Mineral. Petrol. 80, 324-333.

Gascoyne, M., 1992. Geochemistry of the actinides and their daughters. In: Ivanovich, M., Harmon, R.S. (Eds.), Uranium-series disequilibrium: Applications to Earth, Marine, and Environmental Sciences, second ed. Clarendon Press, Oxford, pp. 34-61.

Gascoyne, M., Miller, N.H., Norman, J.A., 2002. Uranium-series isotopic disequilibrium in tuffs from Yucca Mountain, Nevada, as evidence of pore-fluid flow over the last 10^6 a. Appl. Geochem. this issue.

Gerstenberger, H., Haase, G., 1997. A highly effective emitter substance for mass spectrometric Pb isotope ratio determinations. Chem. Geol. 136, 309-312.

Heaney, P.J., 1993. A proposed mechanism for the growth of chalcedony. Contrib. Mineral. Petrol. 115, 66-74.

Herdianita, N.R., Browne, P.R.L., Rogers, K.A., Campbell, K.A., 2000. Mineralogical and textural changes accompanying ageing of silica sinter. Mineral. Depos. 35, 48-62.

Hill, C.A., Dublyansky, Y.V., 1999. Response to Stuckless and others (1998) on "Overview of calcite/opal deposits at or near the proposed high-level nuclear waste site, Yucca Mountain, Nevada, USA: Pedogenic, hypogene, or both?" Environ. Geol. 38, 77-81.

Jaffey, A.H., Flynn, K.F., Glendenin, L.F., Bentley, W.C., Essling, A.M., 1971. Precision measurements of half-lives and specific activities of ^{235}U and ^{238}U. Phys. Rev. C 4, 1889-1906.

Jones, J.B., Segnit, E.R., 1971. The nature of opal. 1. Nomenclature and constituent phases. J. Geol. Soc. Australia 18, 57-68.

Kano, K., 1983. Ordering of opal-CT in diagenesis. Geochem. J. 17, 87-93.

Kigoshi, K., 1971. Alpha-recoil ^{234}Th: Dissolution into water and the uranium-234/uranium-238 disequilibrium in nature. Science 173, 47-48.

Lounsbury, M., Durham, R.W., 1971. The alpha half-life of U-234. In: Hurrel , M.L. (Ed.), Proc. Intl. Conf. Chem. Nucl. Data, Measurement and Applications, Canterbury. Inst. Civil Eng., pp. 215-219.

Ludwig, K.R., 1977. Effect of initial radioactive-daughter disequilibrium on U-Pb isotope apparent ages of young minerals. Jour. Research U.S. Geological Survey 5, 663-667.

Ludwig, K.R., 1987. PBDAT for MS-DOS, A computer program for IBM PC compatibles for processing raw Pb-U-Th isotope data. U.S. Geological Survey Open-File Report 88-542, 40 p.

Ludwig, K.R., 1997. ISOPLOT – a plotting and regression program for radiogenic-isotope data, for IBM-PC compatible computers, version 2.90a. July 1997 revision. of U.S. Geological Survey Open-File Report 91-445, 32 p..

Ludwig, K.R., Lindsey, D.A., Zielinski, R.A., Simmons, K.R., 1980. U-Pb ages of uraniferous opal and implication for the history of beryllium, fluorine, and uranium mineralization at Spor Mountain, Utah. Earth Planet. Sci. Lett. 46, 221-232.

Ludwig, K.R., Simmons, K.R., Webster, J.D., 1984. U-Pb isotope systematics and apparent ages of uranium ores, Ambrosia Lake and Smith Lake districts, Grants Mineral Belt, New Mexico. Econ. Geol. 79, 322-337.

Ludwig, K.R., Wallace, A.R., Simmons, K.R., 1985. The Schwartzwalder uranium deposit, II: Age of uranium mineralization and lead isotope constraints on genesis. Econ. Geol. 80, 1858-1871.

Marshall, B.D., Neymark, L.A., Paces, J.B., Peterman, Z.E., Whelan, J.F., 2000. Seepage flux conceptualized from secondary calcite in lithophysal cavities in the Topopah Spring Tuff, Yucca Mountain, Nevada. Society for Mining, Metallurgy, and Exploration Annual Meeting Preprint 00-12, 6 p.

Meadows, J.W., Armani, R.J., Callis, E.L., Essling, A.M., 1980. Half-life of ^{230}Th. Phys. Rev. C 22, 750-754.

Meijer, A., 1992. A strategy for the derivation and use of sorption coefficients in performance assessment calculations for the Yucca Mountain site. Proceedings of the DOE/Yucca Mountain Site Characterization Project Radionuclide Adsorption Workshop. Los Alamos Nat. Lab. Report LA-12325-C, pp. 9-36.

Montazer, P., Wilson, W.E., 1984. Conceptual hydrological model of flow in the unsaturated zone, Yucca Mountain, Nevada. U.S. Geological Survey Water-Resources Investigation Report 84-4345, 55 p.

Murphy, W.M., Shock, E.L., 1999. Environmental aqueous geochemistry of actinides. In: Burns, P.C., Finch, R. (Eds.), Uranium: Mineralogy, Geochemistry and the Environment, Reviews in Mineralogy, vol. 38. Mineralogical Society of America, Washington, DC, pp. 221-253 (Chapter 5).

Neymark, L.A., Amelin, Y.V., Paces, J.B., Peterman, Z.E., 1998. U-Pb age evidence for long-term stability of the unsaturated zone, Yucca Mountain, Nevada. Proceedings of the Ninth Annual International High-Level Radioactive Waste Management Conference, Las Vegas, Nevada, May 11-14, 1998. American Nuclear Society, pp. 85-87.

Neymark, L.A., Amelin, Y.V., Paces, J.B., 2000. ^{206}Pb-^{230}Th-^{234}U-^{238}U and ^{207}Pb-^{235}U geochronology of Quaternary opal, Yucca Mountain, Nevada. Geochim. Cosmochim. Acta 64, 2913-2928.

Neymark, L.A., Paces, J.B., 2000. Consequences of slow growth for ^{230}Th/U dating of Quaternary opals, Yucca Mountain, Nevada, USA. Chem. Geol. 164, 143-160.

Paces, J.B., Ludwig, K.R., Peterman, Z.E., Neymark, L.A., Kenneally, J.M., 1998. Anomalous ground-water ^{234}U/^{238}U beneath Yucca Mountain: evidence of local recharge?

Proceedings of the Ninth Annual International High-Level Radioactive Waste Management Conference, Las Vegas, Nevada, May 11-14, 1998. American Nuclear Society, pp. 185-188.

Paces, J.B., Neymark, L.A., Marshall, B.D., Whelan, J.F., Peterman, Z.E., 1998. Inferences for Yucca Mountain unsaturated zone hydrology from secondary minerals. Proceedings of the Ninth Annual International High-Level Radioactive Waste Management Conference, Las Vegas, Nevada, May 11-14, 1998. American Nuclear Society, pp. 36-39.

Paces, J.B., Neymark, L.A., Persing, H.M., Wooden, J.L., 2000. Demonstrating slow growth rates in opal from Yucca Mountain, Nevada, using microdigestion and ion-probe U-series dating. Abstracts with Programs, Geological Society of America Annual Meeting, Reno, Nevada, p. A 259.

Paces, J.B., Neymark, L.A., Marshall, B.D., Whelan, J.F., Peterman, Z.E., in press. Ages and origins of calcite and opal in the Exploratory Studies Facility tunnel, Yucca Mountain, Nevada. U.S. Geological Survey Water-Resources Investigations Report 01-4049 (*in press).*

Sawyer, D.A., Fleck, R.J., Lanphere, M.A., Warren, R.G., Broxton, D.E., 1994. Episodic volcanism in the Miocene southwest Nevada volcanic field - stratigraphic revisions, $^{40}Ar/^{39}Ar$ geochronologic framework, and implications for magmatic evolution. GSA Bulletin 106, 1304-1318.

Scott, R.B., Bonk, J., 1984. Preliminary geologic map of Yucca Mountain, Nye County, Nevada, with geologic sections. U.S. Geological Survey Open-File Report 84-494, 9 p., map scale 1:12,000.

Stuckless, J.S., Dudley, W.W., 2001. The geohydrologic setting of Yucca Mountain, Nevada. Appl. Geochem., this issue.

Szillard, L., Chalmers, T.A., 1934. Chemical separation of the radioactive element from its bombarded isotope in the Fermi effect. Nature 134, 462.

Thiry, M., Millot, G., 1987. Mineralogical forms of silica and their sequence of formation in silcretes. J. Sediment. Petrol. 57, 343-352.

Thompson, R.A., 1991. Pliocene environments and climates in the Western United States. Quaternary Sci. Rev. 10, 115-132.

U.S. Department of Energy, 1988. Site characterization plan, Yucca Mountain site, Nevada Research and Development area, Nevada. Office of Civilian Radioactive Waste Management, DOE/RW-0199, 9 vol., variously paged.

Walter, H.J., Rutgers van der Loeff, M.M., Hoeltzen, H., 1997. Enhanced scavenging of ^{231}Pa relative to ^{230}Th in the South Atlantic south of the Polar Front: Implications for the use of the ^{231}Pa/^{230}Th ratio as a paleoproductivity proxy. Earth Planet. Sci. Lett. 149, 85-100.

Whelan, J., Paces, J., Neymark, L., Marshall, B., Peterman, Z., Moscati, R., 2000. Calcite fluid inclusion, paragenetic, and oxygen isotopic records of thermal event(s) at Yucca Mountain, Nevada. Abstracts with Program, Geological Society of America Annual Meeting, Reno, Nevada, p. A 258.

Wilson, N.S.F., Cline, J.S., Rotert, J., Amelin, Y.V., 2000. Timing and temperature of fluid movement at Yucca Mountain, NV: fluid inclusion analyses and U-Pb and U-series dating. Abstracts with Programs, Geological Society of America Annual Meeting, Reno, Nevada, p. A 259.

WoldeGabriel, G., 1995. K-Ar dating of clinoptiolite and coexisting illite/smectite from Yucca Mountain, Nevada. In: Ming, D.W., Mumpton, F.A. (Eds.), Natural zeolites 93 Occurrence, Properties, Use. Int. Comm. On Natural Zeolites, Brockport, New York, pp. 141-156.

Zielinski, R.A., 1982. Uraniferous opal, Virgin Valley, Nevada: Conditions of formation and implications for uranium exploration. J. Geochem. Explor. 16, 197-216.

Figure Captions

Figure 1. a) Map showing Yucca Mountain and the plan view of the Exploratory Studies Facility (ESF) tunnel (after Scott and Bonk, 1984). b) Sampling sites in the Exploratory Studies Facility (ESF) tunnel shown relative to the depth below land surface (W.P. Zelinski and R.W. Clayton, 1996, written communication). Hydrogeologic units exposed in the tunnel (TCw, PTn, and TSw) also are shown. Vertical lines between the units represent faults and contacts.

Figure 2. Concordia diagram showing $^{207}Pb^*/^{235}U$ plotted against $^{206}Pb^*/^{238}U$ for the ESF silica subsamples. Concordia curves correspond to initial $[^{234}U/^{238}U]$ (designated as U_i) 1, 4, and 8. It is assumed that ^{230}Th, ^{231}Pa, and ^{227}Ac were initially absent. U-Pb isotope data are shown with 2σ error ellipses. Note that for ages <10 Ma concordia for $U_i = 1$ coincides with a nearly straight line intersecting the origin of the coordinates.

Figure 3. Line drawing showing $^{207}Pb^*/^{235}U$ ages (Ma) for opal subsamples (outlined hatched areas) collected from different microstratigraphic layers in samples HD2019A and HD2019A1.

Figure 4. Line drawing showing $^{207}Pb^*/^{235}U$ ages (Ma) for opal subsamples (outlined hatched areas) collected from different microstratigraphic layers in samples (a) HD2019, (b) HD2055, (c) HD2059, and (d) HD2074. For HD2019U5, the $^{230}Th/U$ age is shown (Paces *et al.*, 2001). The $^{207}Pb^*/^{235}U$ ages for HD2055Pb1 and HD2059Pb3 are from Neymark *et al.* (2000). For HD2074UPb11a, the $^{230}Th/U$ age (0.242 Ma, this paper) also is shown.

Figure 5. Photograph showing $^{207}Pb^*/^{235}U$ ages (Ma) for subsamples (outlined areas) collected from different microstratigraphic layers in sample HD2357. Areas with abundant calcite (Cc) and opal (Op) also are labeled.

Figure 6. Line drawing showing $^{207}Pb^*/^{235}U$ ages (Ma) for silica subsamples (outlined hatched areas) collected from different microstratigraphic layers in samples (a) HD1838 and (b) HD2257.

Figure 7. Concordia diagram for samples (a) HD2257 and (b) HD2021. Two concordia curves for initial $^{234}U/^{238}U$ activity ratios U_i=1 (equilibrium) and U_i=10 (disequilibrium) are shown. Curved discordia lines correspond to the case of simultaneous Pb and Rn loss when the ratio of their diffusion coefficients $D_{Rn}/D_{Pb} = 5x10^8$. Areas are shaded where the data points would plot if no loss of U decay products occurred. U-Pb isotope data are shown with 2σ error ellipses.

Figure 8. Line drawing showing $^{207}Pb^*/^{235}U$ ages (Ma) for silica subsamples (outlined hatched areas) collected from different microstratigraphic layers in sample HD2021Pb1.

Figure 9. Histogram showing the distribution of $^{207}Pb^*/^{235}U$ ages for the fracture- and cavity-coating silica subsamples from the ESF. Data plotted are combined from this paper (inner silica layers) and from Neymark *et al.* (2000) (opal from outermost surfaces of the coatings).

Figure 10. Relations between $^{207}Pb^*/^{235}U$ ages and relative depths of sampling (2σ error boxes) for silica samples collected from the thickest calcite and silica crusts coating floors of lithophysal cavities in the TSw unit. Solid lines show microstratigraphic order of subsamples. Also given are calculated long-term average rates of the mineral deposition. Parameters of the dashed regression lines were calculated using actual errors for both X and Y values by the ISOPLOT program (Ludwig, 1997).

Figure 11. Relations between $^{207}Pb^*/^{235}U$ ages and relative depths of sampling (2σ error ellipses) for silica samples collected from the UZ at Yucca Mountain (a) above and PTn (b) below the PTn unit. Also given is the calculated long-term average rate of deposition for sample HD1838.

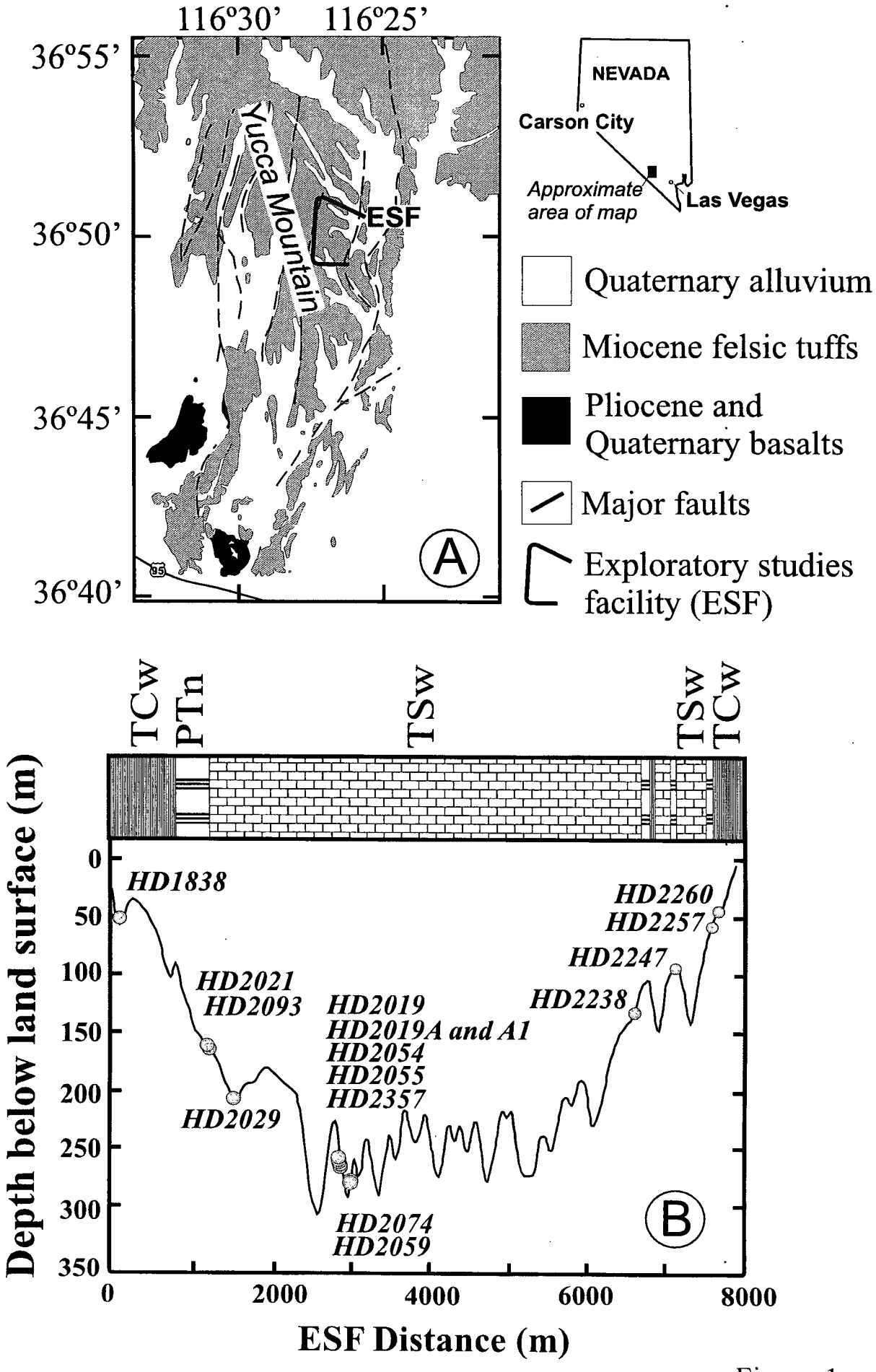
116°30'
116°25'
36°55'
36°50'
36°45'
36°40'
Yucca Mountain
ESF
A
NEVADA
Carson City
Approximate area of map
Las Vegas
Quaternary alluvium
Miocene felsic tuffs
Pliocene and Quaternary basalts
Major faults
Exploratory studies facility (ESF)
TCw
PTn
TSw
TSw
TCw
HD1838
HD2021
HD2093
HD2029
HD2019
HD2019A and A1
HD2054
HD2055
HD2357
HD2074
HD2059
HD2260
HD2257
HD2247
HD2238
B
Depth below land surface (m)
0
50
100
150
200
250
300
350
0
2000
4000
6000
8000
ESF Distance (m)

Figure 1

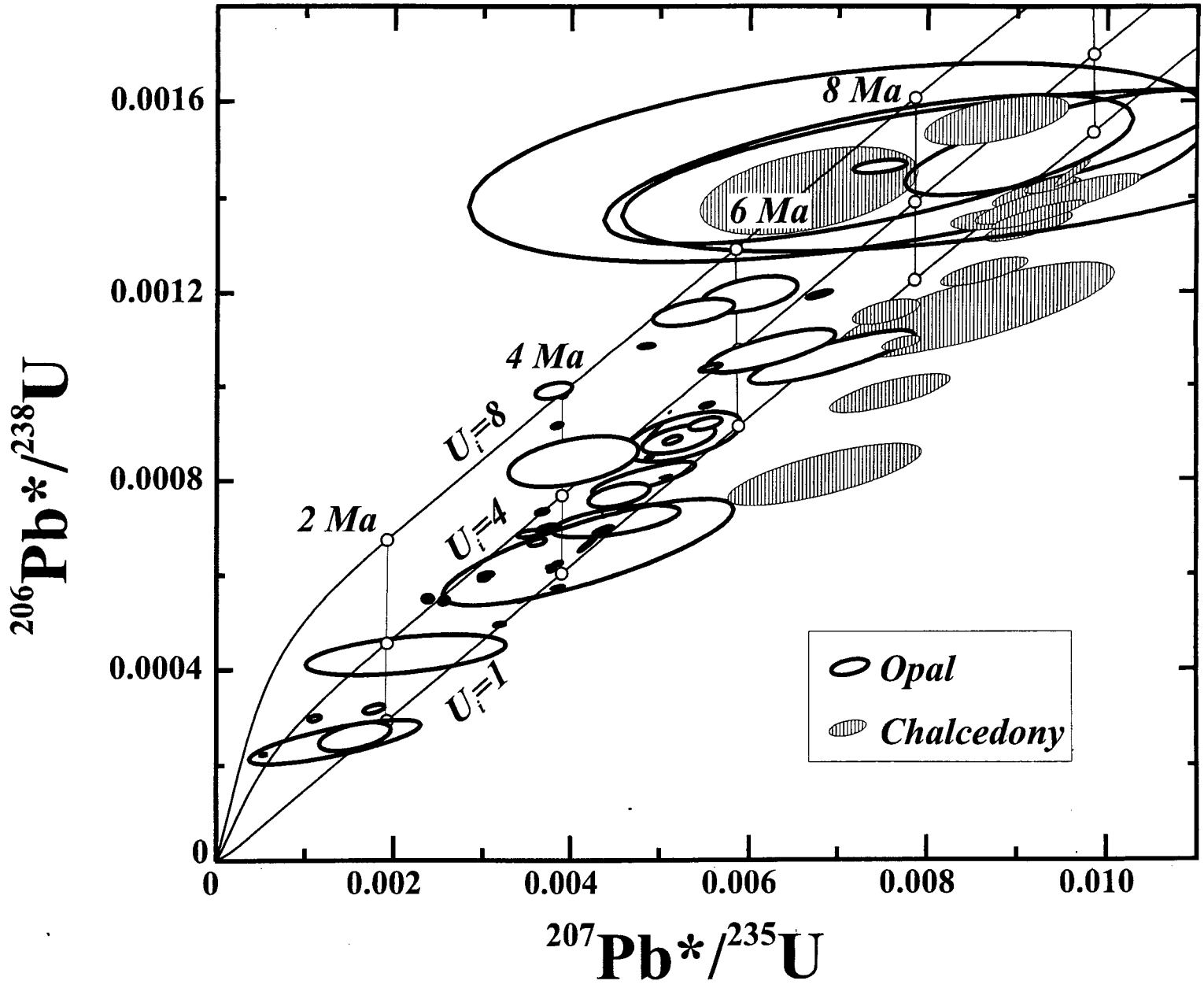

Figure 2
(Neymark et al.)

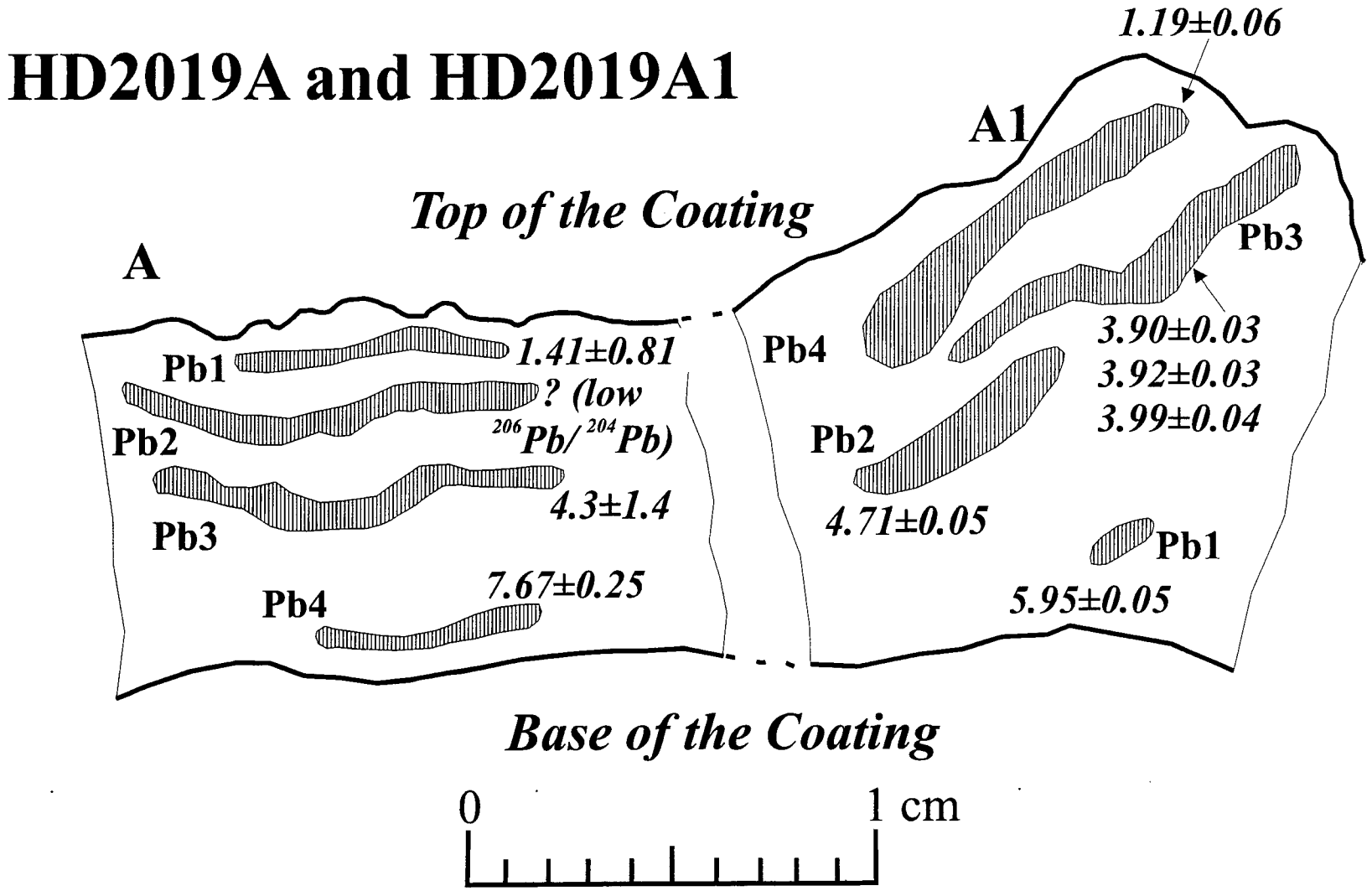

Figure 3
(Neymark et al.)

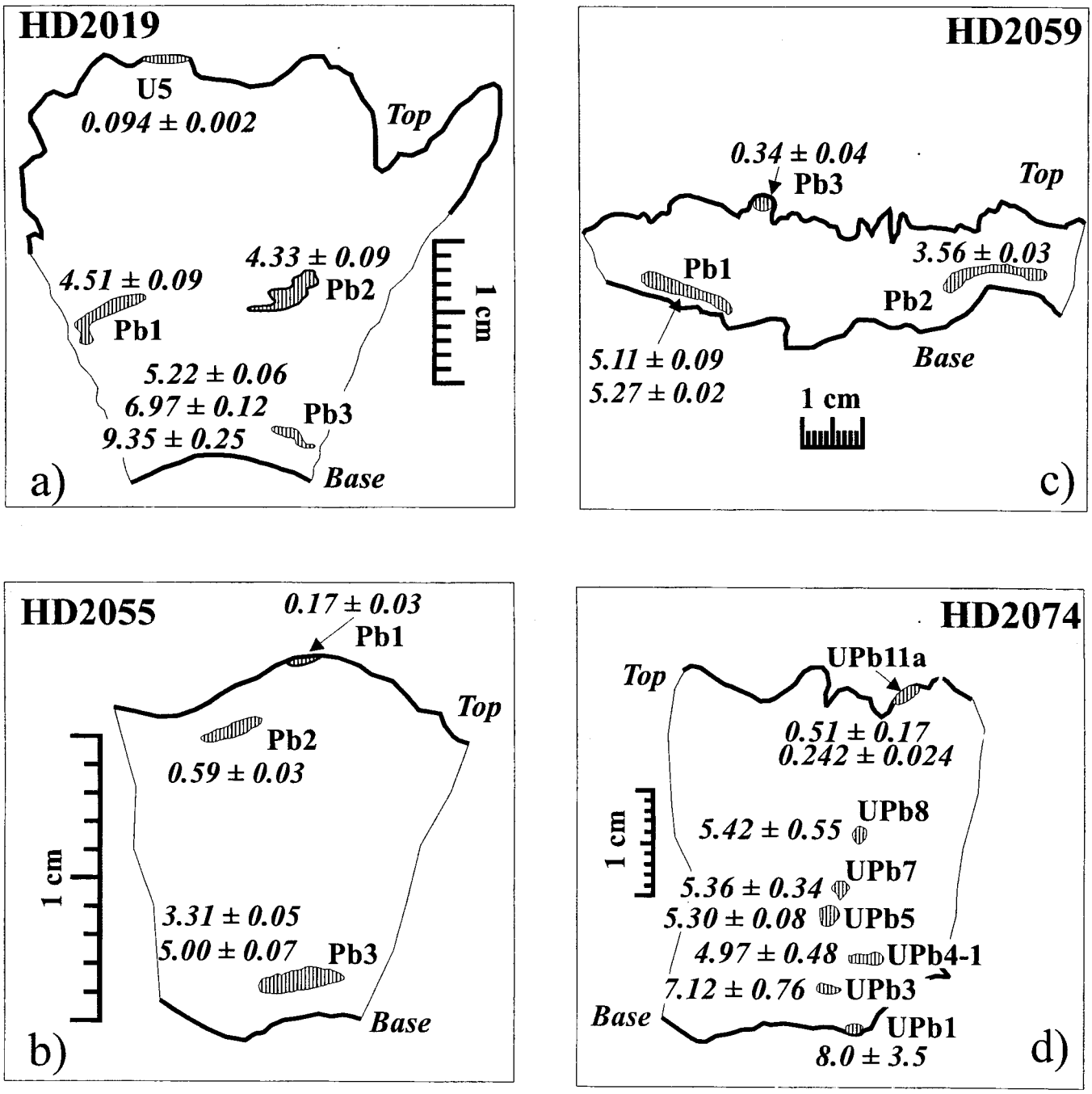

Figure 4
(Neymark et al.)

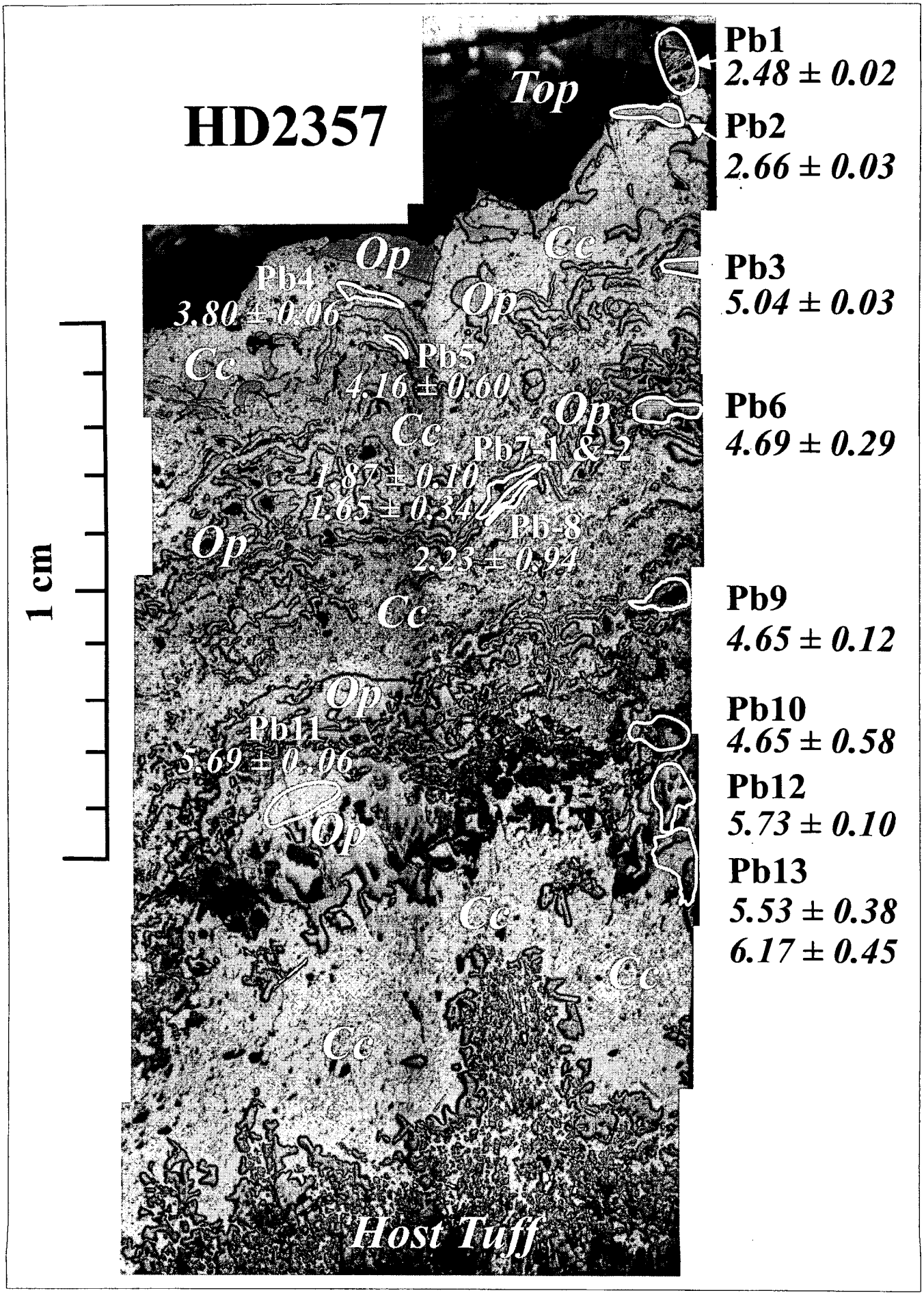

Figure 5
(Neymark et al.)

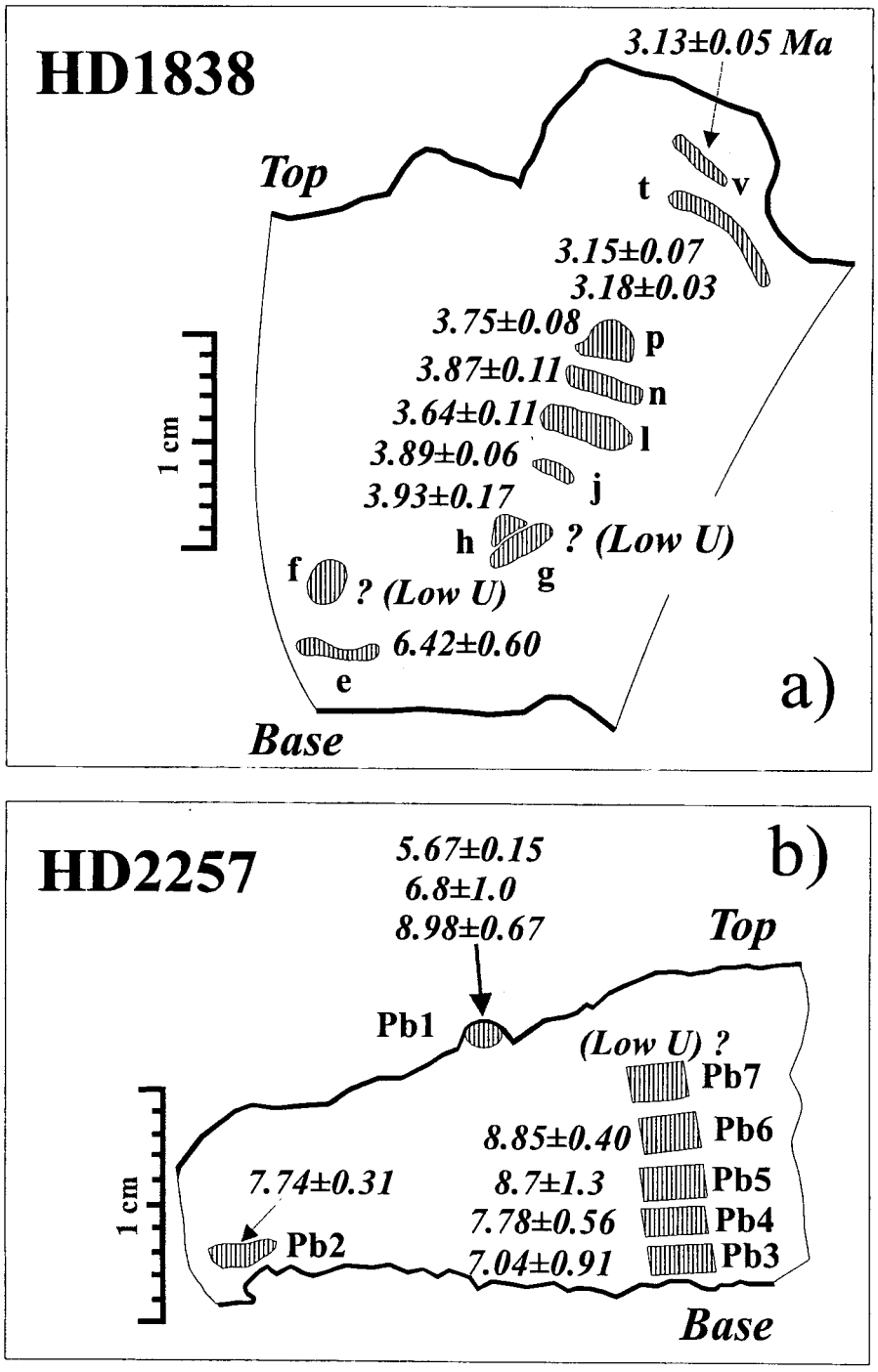

Figure 6
(Neymark et al.)

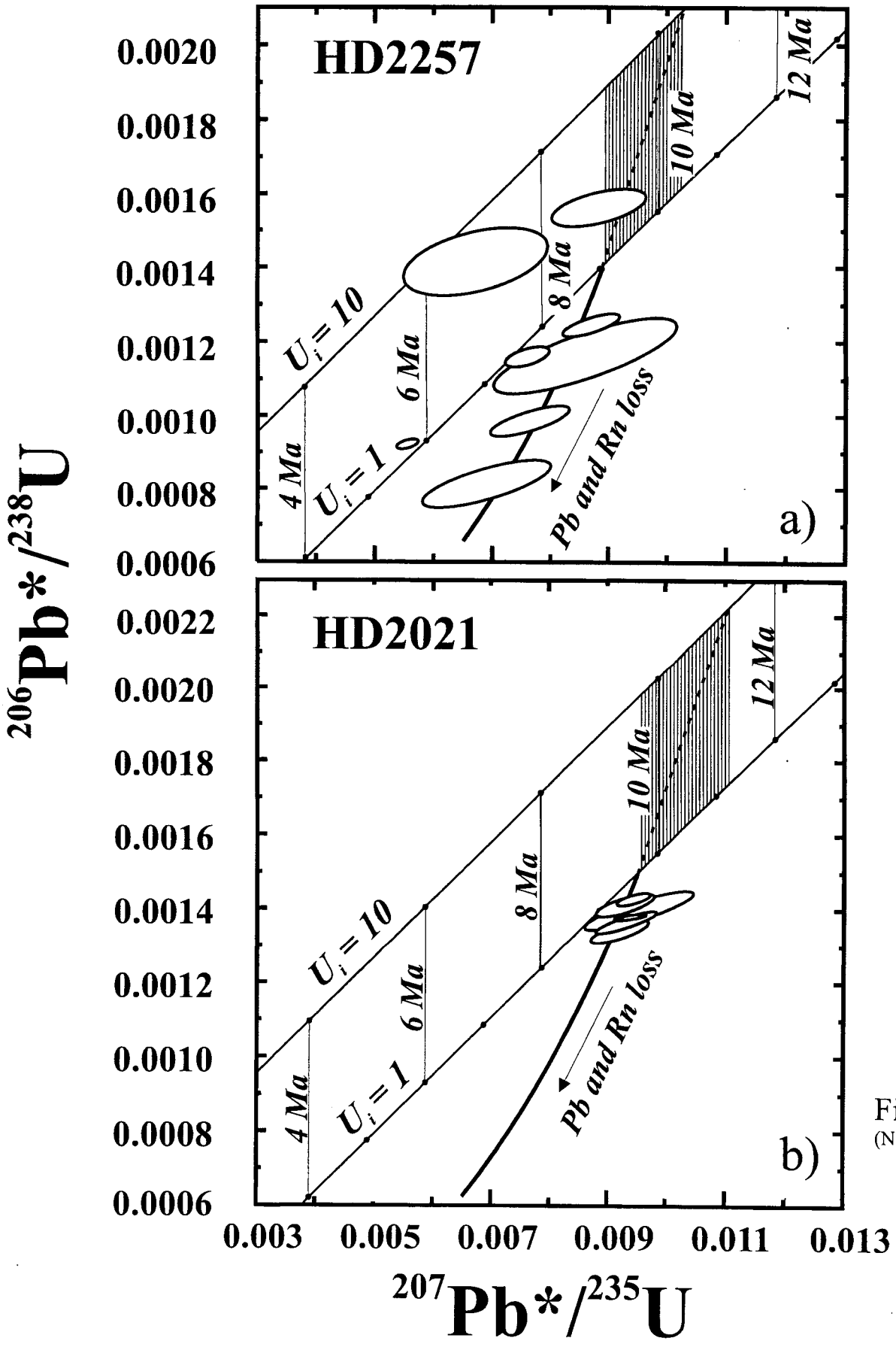

Figure 7
(Neymark et al.)

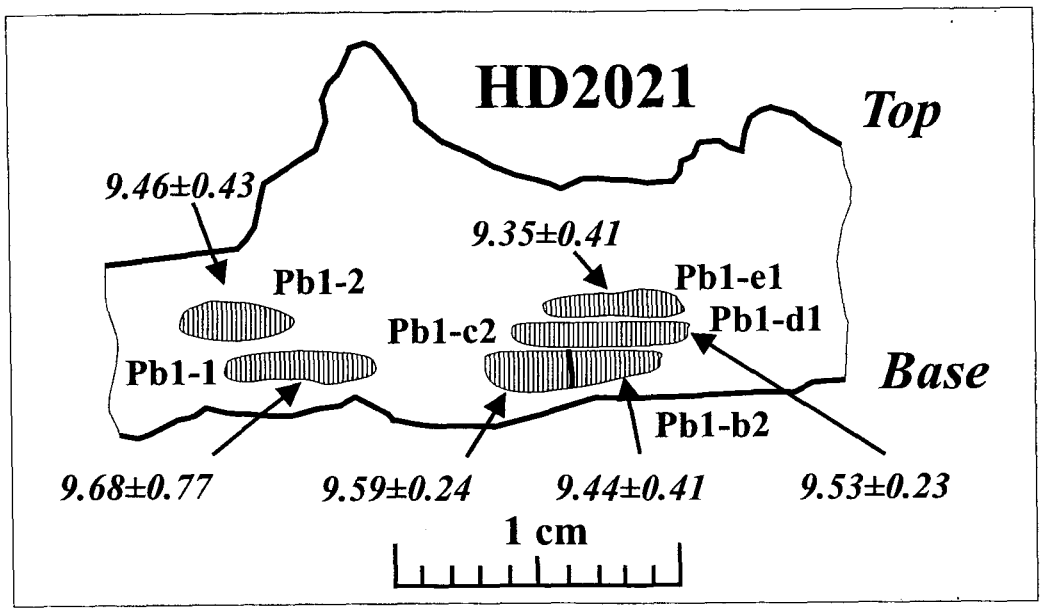

Figure 8
(Neymark et al.)

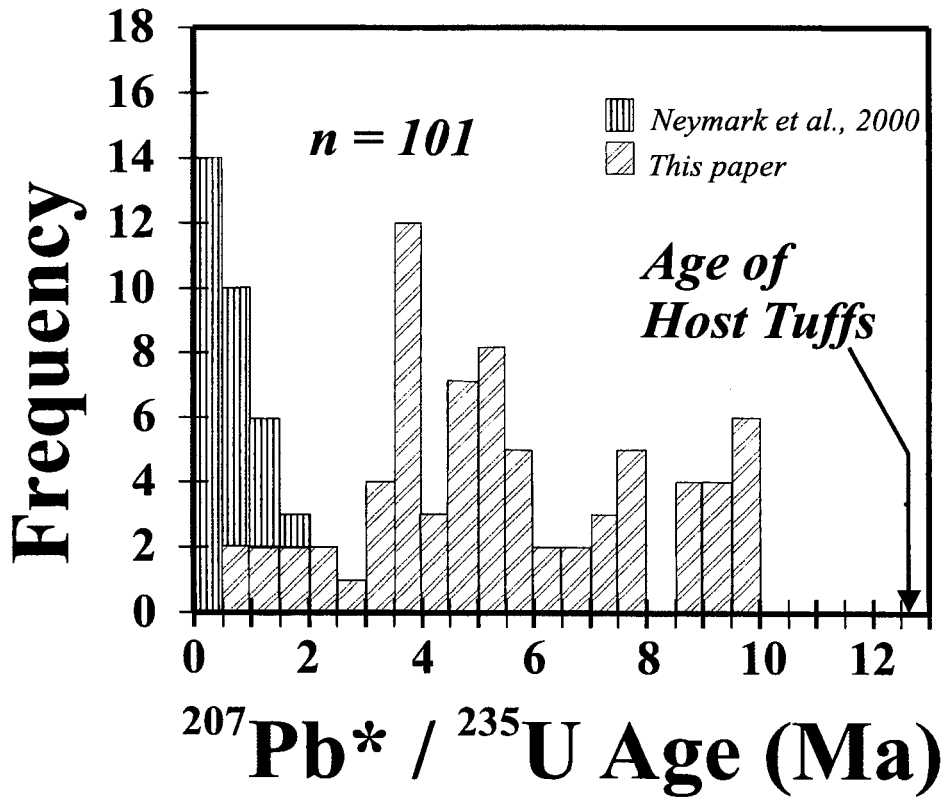

Figure 9
(Neymark et al.)

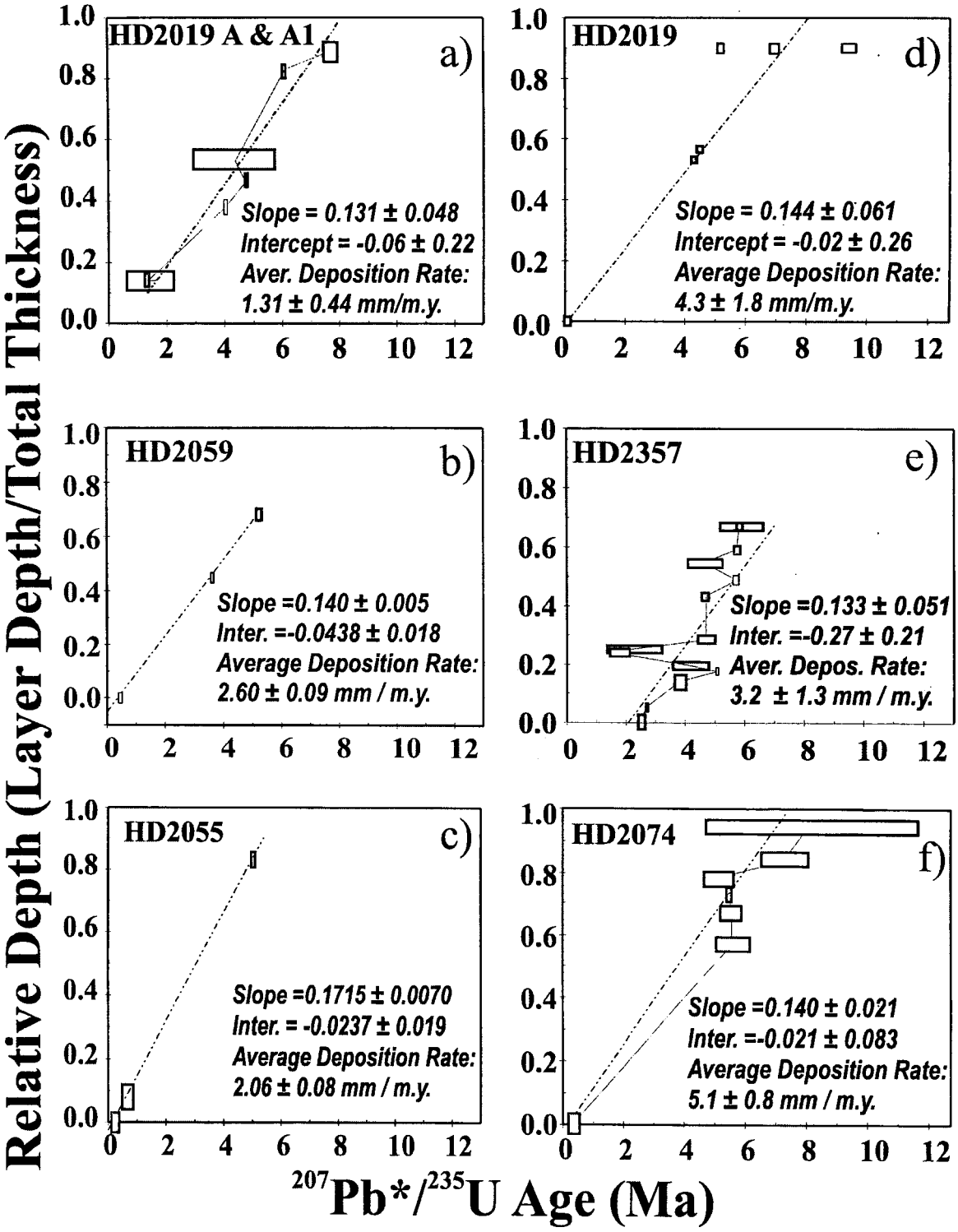

Figure 10
(Neymark et al.)

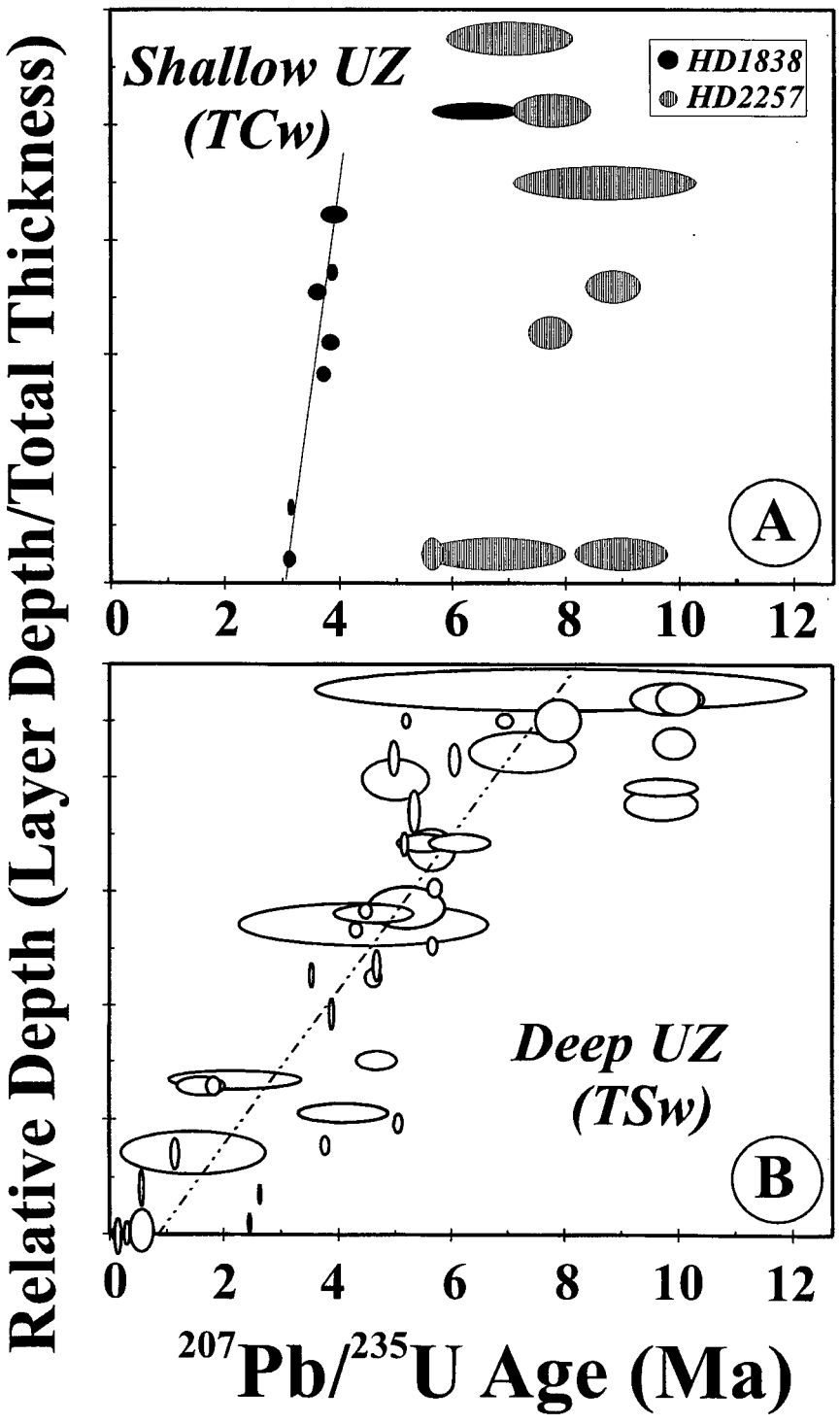

Figure 11
(Neymark et al.)

Table 1: Measured U-Th-Pb isotope data for silica samples from the Exploratory Studies Facility, Yucca Mountain, Nevada

Subsample Name	Mineral	Occurrence	ESF Distance (m)	Host Rock	Weight (mg)	U (ppm)	Pb (ppb)	Th (ppb)	$^{206}Pb/^{204}Pb$[a]	Error (%)	$^{207}Pb/^{204}Pb$[a]	Error (%)	$^{208}Pb/^{204}Pb$[a]	Error (%)	$^{238}U/^{204}Pb$[a]	$^{234}U/^{238}U_{act.}$[b]	Error	$^{230}Th/^{238}U_{act.}$[b]	Error
HD1838e	Opal	Fracture	111.55	TCw	4.013	5.98	23.2	37.9	42.60	0.73	16.63	0.24	39.22	0.28	2.208E+04	1.019	0.014	0.998	0.027
HD1838f	Opal	"	"	"	2.016	2.63	71.6	76.5	73.77	0.79	15.77	0.20	39.46	0.28	4.114E+03	0.992	0.007	1.021	0.015
HD1838g	Opal	"	"	"	0.726	1.47	14.9	299	29.55	3.69	16.14	1.06	39.14	1.2	7.347E+03	0.981	0.012	0.977	0.016
HD1838h	Opal	"	"	"	0.384	43.7	50.8	10.4	244.2	16.50	21.93	5.58	39.69	2.4	2.268E+05	0.951	0.022	1.05	0.14
HD1838j	Opal	"	"	"	1.023	47.5	34.0	3.38	539.8	19.40	35.99	11.60	40.08	2.6	7.406E+05	1.002	0.004	1.001	0.008
HD1838l	Opal	"	"	"	0.837	45.9	31.6	0.47	587.8	27.5	36.87	16.8	34.10	4.5	8.258E+05	1.017	0.003	1.028	0.011
HD1838n	Opal	"	"	"	0.826	37.1	25.7	1.68	660.7	38.4	40.75	24.8	38.86	4.9	9.179E+05	1.033	0.006	1.055	0.009
HD1838p	Opal	"	"	"	0.632	59.5	38.3	95.2	1018.5	51.10	55.02	37.6	39.19	6.1	1.488E+06	1.032	0.004	1.049	0.007
HD1838t-1	Opal	"	"	"	1.945	63.1	35.9	0.66	1094.3	18.90	55.87	14.0	38.95	2.3	1.796E+06	1.022	0.005	1.025	0.005
HD1838t-2	Opal	"	"	"	1.000	52.9	35.2	3.81	315.8	11.60	26.57	5.32	38.51	1.5	4.930E+05	1.034	0.005	1.036	0.006
HD1838v	Opal	"	"	"	1.256	56.7	32.8	5.71	808.4	23.9	44.88	16.3	38.65	3.1	1.326E+06	1.018	0.005	1.019	0.007
HD2019A1Pb1	Opal	Cavity	2880.0	TSw	1.599	65.8	73.2	6.12	368.4	4.03	29.93	2.11	38.53	0.57	3.385E+05	1.004	0.006	1.000	0.007
HD2019A1Pb2	Opal	"	"	"	1.580	86.2	76.5	1.08	241.8	2.67	25.57	1.20	39.21	0.54	2.983E+05	1.003	0.007	1.003	0.005
HD2019A1Pb3-1	Opal	"	"	"	2.309	187	129	2.46	299.3	1.33	28.28	0.71	39.06	0.37	4.571E+05	1.016	0.006	1.068	0.084
HD2019A1Pb3-2	Opal	"	"	"	1.469	164	117	1.97	283.1	2.20	27.51	1.14	39.00	0.58	4.217E+05	1.010	0.002	1.009	0.004
HD2019A1Pb3-3	Opal	"	"	"	1.091	166	113	147	347.1	3.65	30.25	1.94	39.17	0.55	5.298E+05	1.017	0.006	1.031	0.005
HD2019A1Pb4	Opal	"	"	"	0.393	117	32.7	<10	1668.1	154.0	60.24	117.0	46.85	36.8	5.479E+06	1.335	0.007	1.340	0.011
HD2019APb1	Opal	Cavity	2880.0	TSw	0.790	21.8	58.7	n.d.	25.37	1.1	15.87	0.59	38.86	0.48	2.601E+04	1.278	0.047	n.d.	n.d.
HD2019APb1 L[c]	Opal	"	"	"	0.620	3.18	296	n.d.	21.72	0.28	15.67	0.26	38.35	0.31	7.126E+02	0.90	0.29	n.d.	n.d.
HD2019APb2	Opal	"	"	"	0.510	13.5	3136	n.d.	18.95	0.16	15.66	0.20	38.73	0.26	2.767E+02	1.027	0.148	n.d.	n.d.
HD2019APb2 L[c]	Opal	"	"	"	1.090	0.622	1350	n.d.	19.22	0.16	15.68	0.20	38.69	0.27	2.969E+01	n.d.	n.d.	n.d.	n.d.
HD2019APb3	Opal	"	"	"	3.830	26.3	256	n.d.	23.35	0.35	15.83	0.37	38.28	0.96	6.961E+03	0.97	0.24	n.d.	n.d.
HD2019APb3 L[c]	Opal	"	"	"	0.880	0.551	454	n.d.	18.36	0.25	15.59	0.27	38.01	0.42	7.646E+01	n.d.	n.d.	n.d.	n.d.
HD2019APb4	Opal	"	"	"	1.170	28.9	45.5	n.d.	372	14	28.8	7.0	39.16	3.0	2.408E+05	0.974	0.024	n.d.	n.d.
HD2019APb4 L[c]	Opal	"	"	"	0.690	0.273	51.4	n.d.	29.82	1.9	15.69	0.88	38.39	1.3	3.892E+02	n.d.	n.d.	n.d.	n.d.
HD2019Pb1	Opal	Cavity	2881.0	TSw	25.40	63.5	59.1	n.d.	167.1	0.16	22.42	0.14	39.37	0.15	2.128E+05	1.002	0.006	n.d.	n.d.
HD2019Pb2	Opal	"	"	"	11.45	270	193	n.d.	391.4	0.20	32.75	0.15	39.24	0.16	5.583E+05	0.994	0.007	n.d.	n.d.
HD2019Pb3-1	Opal	"	"	"	7.010	44.0	64.8	n.d.	211.7	0.50	23.61	0.24	39.43	0.23	1.609E+05	0.990	0.003	n.d.	n.d.
HD2019Pb3-2	Opal	"	"	"	13.77	6.56	17.8	n.d.	181.6	0.79	20.76	0.31	39.72	0.25	7.697E+04	0.997	0.008	n.d.	n.d.
HD2019Pb3-3	Opal	"	"	"	3.151	194	179	n.d.	284.7	1.0	27.79	0.57	39.06	0.39	3.284E+05	1.000	0.006	n.d.	n.d.
HD2021Pb1-1	Chalc.	Fracture	1221.83	TSw	42.28	10.2	42.3	n.d.	50.17	0.21	17.17	0.22	39.24	0.26	2.243E+04	0.995	0.027	n.d.	n.d.
HD2021Pb1-2	Chalc.	"	"	"	43.53	11.5	32.7	n.d.	73.18	0.22	18.31	0.22	39.18	0.29	3.981E+04	1.000	0.054	n.d.	n.d.
HD2021Pb1-b1	Quartz	"	"	"	1.817	0.045	6.15	n.d.	19.92	1.2	15.73	0.91	39.29	1.8	4.855E+02	n.d.	n.d.	n.d.	n.d.
HD2021Pb1-b2	Chalc.	"	"	"	4.435	7.11	23.1	n.d.	65.85	0.999	17.82	0.29	39.28	0.30	3.263E+04	n.d.	n.d.	n.d.	n.d.

Table 1 (Continued)

Subsample Name	Mineral	Occurrence	ESF Distance (m)	Host Rock	Weight (mg)	U (ppm)	Pb (ppb)	Th (ppb)	$^{206}Pb/^{204}Pb^{a}$	Error (%)	$^{207}Pb/^{204}Pb^{a}$	Error (%)	$^{208}Pb/^{204}Pb^{a}$	Error (%)	$^{238}U/^{204}Pb^{a}$	$^{234}U/^{238}U_{act.}{}^{b}$	Error	$^{230}Th/^{238}U_{act.}{}^{b}$	Error
HD2021Pb1-c1	Quartz	"	"	"	1.753	0.067	6.01	n.d.	19.77	1.23	15.61	0.86	39.02	1.1	7.209E+02	n.d.	n.d.	n.d.	n.d.
HD2021Pb1-c2	Chalc.	"	"	"	2.747	11.1	25.7	n.d.	108.2	2.26	19.91	0.70	39.06	0.42	6.262E+04	n.d.	n.d.	n.d.	n.d.
HD2021Pb1-d1	Chalc.	Fracture	1221.83	TSw	5.671	12.7	29.0	n.d.	103.9	0.96	19.78	0.37	39.11	0.31	6.174E+04	n.d.	n.d.	n.d.	n.d.
HD2021Pb1-e1	Chalc.	"	"	"	3.687	13.6	43.9	n.d.	61.39	0.60	17.74	0.21	38.82	0.25	3.175E+04	n.d.	n.d.	n.d.	n.d.
HD2029Pb1-1	Chalc.	Fracture	1533.25	TSw	1.620	12.3	17.7	n.d.	409	14	34.05	8.3	39.35	3.0	2.876E+05	1.002	0.008	n.d.	n.d.
HD2029Pb2-1	Chalc.	"	"	"	34.64	72.4	114	n.d.	376.5	0.35	32.94	0.34	39.06	1.1	2.464E+05	1.000	0.005	n.d.	n.d.
HD2054Pb1	Opal	Cavity	2881.6	TSw	1.373	192	133	n.d.	236.4	2.7	26.28	1.3	39.13	0.67	3.778E+05	0.998	0.006	n.d.	n.d.
HD2055Pb2	Opal	Cavity	2911.2	TSw	1.070	148	29.5	n.d.	5878	82	116	72	42.26	19	2.594E+07	1.821	0.009	n.d.	n.d.
HD2055Pb3-1	Opal	"	"	"	0.710	150	146	n.d.	23834	205	792	201	58.29	84	2.189E+07	1.003	0.006	n.d.	n.d.
HD2055Pb3-2	Opal	"	"	"	0.429	382	187	n.d.	808	9.5	52.6	7.0	39.87	2.2	1.584E+06	0.949	0.007	n.d.	n.d.
HD2059Pb1-1	Opal	Cavity	3017.78	TSw	1.620	475	387	n.d.	35167	50	1418	50	44.15	13	3.870E+07	0.998	0.006	n.d.	n.d.
HD2059Pb1-2	Opal	"	"	"	3.775	188	159	n.d.	53806	80	2142	80	46.69	23	5.687E+07	1.002	0.006	n.d.	n.d.
HD2059Pb2	Opal	"	"	"	2.835	293	169	n.d.	430.1	1.8	34.51	1.1	39.28	0.53	7.525E+05	0.997	0.005	n.d.	n.d.
HD2074UPb1	Opal	Cavity	3050.7	TSw	0.160	7.61	41.8	91.7	41.7	14.5	16.51	2.9	39.31	3.0	1.547E+04	1.506	0.035	n.d.	n.d.
HD2074UPb2	Opal	"	"	"	2.583	33.3	n.d.	7.13	n.d.	n.d.	n.d.	n.d.	n.d.	n.d.	n.d.	1.025	0.005	1.006	0.055
HD2074UPb3-1	Opal	"	"	"	0.690	45.6	207	n.d.	38.03	1.22	16.535	0.32	39.18	0.33	1.806E+04	n.d.	n.d.	n.d.	n.d.
HD2074UPb3-2	Opal	"	"	"	3.006	49.4	n.d.	15.2	n.d.	n.d.	n.d.	n.d.	n.d.	n.d.	n.d.	1.017	0.003	n.d.	n.d.
HD2074UPb4-1	Opal	"	"	"	1.750	75.5	220	n.d.	42.50	0.58	16.66	0.3	39.12	0.3	2.938E+04	n.d.	n.d.	n.d.	n.d.
HD2074UPb4-2	Opal	"	"	"	3.427	35.9	n.d.	7.15	n.d.	n.d.	n.d.	n.d.	n.d.	n.d.	n.d.	1.008	0.006	0.994	0.036
HD2074UPb5	Opal	"	"	"	0.035	780	628	141	5743	232	258	219	40.65	32	6.451E+06	1.042	0.011	1.018	0.046
HD2074UPb6	Opal	"	"	"	0.006	8.45	271	n.d.	19.8	13.2	15.92	8.1	40.01	12	n.d.	n.d.	n.d.	n.d.	n.d.
HD2074UPb7	Opal	"	"	"	0.160	80.3	98.1	29.9	154	20.6	21.42	6.9	38.9	2.6	1.522E+05	1.050	0.017	1.002	0.041
HD2074UPb8	Opal	"	"	"	0.055	141	146	0.11	274	67.9	26.63	31	40.6	9.8	2.861E+05	1.095	0.014	1.009	0.050
HD2074UPb9[d]	Opal	"	"	"	0.167	n.d.	n.d.	n.d.	2991	0.73	140.4	0.84	37.88	1.0	n.d.	0.981	0.002	n.d.	n.d.
HD2074UPb10[d]	Opal	"	"	"	0.044	n.d.	n.d.	n.d.	204.8	0.58	23.33	0.72	37.95	0.6	n.d.	1.006	0.009	n.d.	n.d.
HD2074UPb11[d]	Opal	"	"	"	2.430	n.d.	n.d.	n.d.	631	2.5	24.28	3.6	37.9	3.1	n.d.	2.765	0.002	n.d.	n.d.
HD2074UPb11a	Opal	"	"	"	0.302	164	67.5	4.41	69.5	15.7	16.485	2.4	39.1	2.4	2.635E+05	2.659	0.021	2.777	0.097
HD2093Pb1	Opal	Fracture	1215.58	TSw	0.086	119	1004	n.d.	32.62	0.33	16.25	0.23	39.05	0.27	9.107E+03	1.015	0.007	n.d.	n.d.
HD2238Pb1	Opal	Fracture	6600	TSw	0.732	3.01	34.0	n.d.	28.31	0.83	15.97	0.46	39.52	2.3	6.492E+03	0.995	0.010	n.d.	n.d.
HD2247APb1	Opal	Fracture	7165.8	TSw	0.713	50.7	47.0	n.d.	550	10	31.89	5.5	39.92	1.5	5.788E+05	1.024	0.005	n.d.	n.d.

Table 1 (Continued)

Subsample Name	Mineral	Occurrence	ESF Distance (m)	Host Rock	Weight (mg)	U (ppm)	Pb (ppb)	Th (ppb)	$^{206}Pb/^{204}Pb$[a]	Error (%)	$^{207}Pb/^{204}Pb$[a]	Error (%)	$^{208}Pb/^{204}Pb$[a]	Error (%)	$^{238}U/^{204}Pb$[a]	$^{234}U/^{238}U_{act.}$[b]	Error	$^{230}Th/^{238}U_{act.}$[b]	Error
HD2257Pb1-1	Opal	Fracture	7506.8	TCw	0.393	56.9	61.4	16.0	266.7	14.7	26.46	6.80	43.14	2.97	2.690E+05	1.012	0.014	1.009	0.012
HD2257Pb1-2	Chalc.	"	"	"	0.804	6.46	21.0	10.9	73.87	6.77	17.88	1.53	40.13	1.23	3.523E+04	1.004	0.013	1.08	0.14
HD2257Pb1-3	Chalc.	"	"	"	0.233	11.6	25.1	13.6	127.14	32.00	19.35	8.42	44.20	7.4	7.655E+04	1.010	0.015	1.09	0.19
HD2257Pb2	Chalc.	"	"	"	0.567	17.4	26.3	21.8	183.3	17.00	23.43	6.71	40.65	2.57	1.417E+05	0.998	0.009	1.007	0.023
HD2257Pb3	Chalc.	"	"	"	0.923	10.1	48.7	10.5	31.43	0.97	16.40	0.30	38.24	0.37	1.551E+04	0.970	0.016	0.972	0.009
HD2257Pb4	Chalc.	"	"	"	1.765	11.0	39.1	51.9	42.47	0.96	16.95	0.28	38.61	0.30	2.399E+04	0.970	0.008	0.989	0.013
HD2257Pb5	Chalc.	"	"	"	4.240	9.31	70.4	278	30.19	0.17	16.23	0.16	38.15	0.22	9.774E+03	1.012	0.057	n.d.	n.d.
HD2257Pb6	Chalc.	"	"	"	3.443	6.61	19.9	189	61.34	1.41	17.78	0.38	38.99	0.36	3.414E+04	0.998	0.014	n.d.	n.d.
HD2257Pb7	Chalc.	Fracture	7506.8	TCw	1.710	2.86	49.7	83.9	29.58	0.50	16.09	0.25	39.40	0.42	4.277E+03	1.012	0.054	n.d.	n.d.
HD2260Pb1	Opal	Fracture	7574.7	TCw	0.141	66.0	81.0	n.d.	313.6	18	30.83	9.7	39.44	2.4	2.698E+05	1.001	0.006	n.d.	n.d.
HD2357Pb1	Opal	Cavity	2828[e]	TSw	1.778	153	86.0	n.d.	513.3	2.1	31.18	1.2	38.41	0.48	8.946E+05	1.048	0.004	n.d.	n.d.
HD2357Pb2	Opal	"	"	"	0.754	167	85.4	n.d.	1667	16	71.83	13	46.22	4.6	3.007E+06	1.049	0.006	n.d.	n.d.
HD2357Pb3	Opal	"	"	"	0.184	337	259	n.d.	8165	101	358	97	39.99	20	9.574E+06	1.002	0.006	n.d.	n.d.
HD2357Pb4	Opal	"	"	"	0.090	322	223	n.d.	1464	44	68.42	35	49.24	12	1.965E+06	1.006	0.005	n.d.	n.d.
HD2357Pb5	Opal	"	"	"	0.015	176	139	n.d.	998	285	49.84	202	21.65	229	1.163E+06	0.987	0.021	n.d.	n.d.
HD2357Pb6	Opal	"	"	"	0.030	189	145	n.d.	679	97	44	65	38.93	12	8.572E+05	0.996	0.011	n.d.	n.d.
HD2357Pb7-1	Opal	"	"	"	0.201	76.3	23.2	n.d.	1151	149	62	114	37.15	23	3.534E+06	1.023	0.006	n.d.	n.d.
HD2357Pb7-2	Opal	"	"	"	0.068	69.3	18.1	n.d.	723	367	46	254	46.15	86	2.682E+06	1.027	0.010	n.d.	n.d.
HD2357Pb8	Opal	"	"	"	0.072	29.9	70.1	n.d.	32.8	4.6	16.1	1.3	37.57	1.8	3.218E+04	1.083	0.014	n.d.	n.d.
HD2357Pb9	Opal	"	"	"	0.132	103	81.5	n.d.	389.2	23	32.2	13	39.15	3.0	5.018E+05	0.993	0.007	n.d.	n.d.
HD2357Pb10	Opal	"	"	"	0.082	57.5	143	n.d.	43.4	2.9	16.75	0.82	38.31	0.75	3.440E+04	0.903	0.009	n.d.	n.d.
HD2357Pb11	Opal	"	"	"	1.181	64.6	70.6	n.d.	284.4	2.3	26.79	1.1	39.16	0.57	2.764E+05	0.995	0.008	n.d.	n.d.
HD2357Pb12	Opal	"	"	"	1.670	42.6	59.1	n.d.	164.5	1.2	21.31	0.46	38.98	0.37	1.399E+05	0.974	0.004	n.d.	n.d.
HD2357Pb13-1	Opal	"	"	"	0.188	26.3	54.5	n.d.	90.50	6.6	18.05	1.5	38.95	2.4	6.180E+04	0.961	0.008	n.d.	n.d.
HD2357Pb13-2	Opal	"	"	"	0.12	29.0	51.6	n.d.	127.5	15	19.60	4.1	39.62	5.3	9.085E+04	0.988	0.009	n.d.	n.d.

[a] Isotopic ratios, corrected for mass-discrimination, spike contribution, and procedure blank.

[b] Activity ratios, calculated from measured isotopic ratios corrected for mass-discrimination, spike contribution, and procedure blank.

[c] Powdered subsamples from sample HD2019A were leached with 2*N* HCl and results are reported for residues and leachates (L).

[d] Unspiked samples (no concentration data).

[e] Sample collected from Alcove #5 at a distance of 28.5 m from the main tunnel.

n.d. - not determined

Table 2: Calculated isotope ratios and U-Pb ages for silica samples from the Exploratory Studies Facility, Yucca Mountain, Nevada

Subsample Name	^{206}*Pb/ ^{238}U[a] (E-3)	Error (%)	^{207}*Pb/ ^{235}U[a] (E-3)	Error (%)	Rho[b] 6/8-7/5	^{207}Pb*/ ^{206}Pb*[a] (E-2)	Error (%)	^{206}Pb*/ ^{238}U Age (Ma)[c]	Error (Ma)	^{207}Pb*/ ^{235}U Age (Ma)[d]	Error (Ma)	^{207}Pb*/ ^{206}Pb* Age (Ma)[c]	^{234}U/ ^{238}U$_{ini}$[e]	Error
HD1838e	1.077	3.5	6.297	9.5	0.76	4.242	7.2	6.94	0.24	6.42	0.60	-202	2.9	1.4
HD1838f	13.35	1.5	5.157	61	0.76	0.280	60	85.5	1.3	5.3	3.2	0	231	6
HD1838g	1.459	9.5	9.664	35	0.55	4.804	31	9.40	0.89	9.8	3.4	101	0.3	5.1
HD1838h	0.993	1.4	3.836	4.5	0.44	2.801	4.1	6.40	0.09	3.93	0.17	-1375	8.45	0.50
HD1838j	0.704	0.73	3.792	1.6	0.55	3.909	1.4	4.53	0.03	3.89	0.06	-411	3.27	0.19
HD1838l	0.689	0.94	3.549	3.0	0.45	3.735	2.7	4.44	0.04	3.64	0.11	-531	3.71	0.24
HD1838n	0.699	1.1	3.775	2.9	0.48	3.916	2.6	4.51	0.05	3.87	0.11	-406	3.24	0.29
HD1838p	0.672	0.96	3.651	2.2	0.53	3.942	1.8	4.33	0.04	3.75	0.08	-389	3.10	0.24
HD1838t-1	0.599	0.55	3.090	0.97	0.62	3.743	0.76	3.86	0.02	3.18	0.03	-526	3.38	0.12
HD1838t-2	0.602	0.79	3.061	2.2	0.51	3.686	1.9	3.88	0.03	3.15	0.07	-567	3.52	0.17
HD1838v	0.595	0.62	3.042	1.6	0.49	3.706	1.4	3.84	0.02	3.13	0.05	-552	3.45	0.13
HD2019A1Pb1	1.033	0.42	5.831	0.91	0.66	4.095	0.71	6.65	0.03	5.95	0.05	-291	3.45	0.16
HD2019A1Pb2	0.748	0.54	4.598	1.1	0.72	4.461	0.82	4.82	0.03	4.71	0.05	-77	1.77	0.15
HD2019A1Pb3-1	0.614	0.46	3.820	0.89	0.72	4.514	0.64	3.95	0.02	3.92	0.03	-48	1.55	0.10
HD2019A1Pb3-2	0.627	0.50	3.887	1.1	0.67	4.499	0.85	4.04	0.02	3.99	0.04	-56	1.60	0.11
HD2019A1Pb3-3	0.620	0.44	3.806	0.87	0.69	4.456	0.65	3.99	0.02	3.90	0.03	-80	1.70	0.10
HD2019A1Pb4	0.301	1.7	1.123	5.2	0.41	2.706	4.8	1.94	0.03	1.19	0.06	-1488	3.74	0.12
HD2019APb1	0.251	15	1.347	59	0.78	3.886	24	1.62[f]	0.24	1.41[f]	0.81	-426	2.1	1.3
HD2019APb3	0.650	14	4.223	32	0.80	4.713	56	4.19[f]	0.57	4.3[f]	1.4	56	n.d.	n.d
HD2019APb4	1.466	0.78	7.532	3.3	0.46	3.726	3.0	9.45	0.07	7.67	0.25	-538	6.50	0.42
HD2019Pb1	0.697	0.95	4.406	2.0	0.81	4.585	1.3	4.49	0.04	4.51	0.09	-10	1.39	0.24
HD2019Pb2	0.667	1.9	4.231	2.0	0.97	4.598	0.53	4.30	0.08	4.33	0.09	-3	1.35	0.46
HD2019Pb3-1	1.197	0.56	6.844	1.7	0.81	4.145	1.2	7.71	0.04	6.97	0.12	-260	3.56	0.25
HD2019Pb3-2[g]	2.115	0.65	9.209	2.7	0.77	3.158	2.2	13.6	0.09	9.35	0.25	-1004	13.6	0.5
HD2019Pb3-3	0.809	0.42	5.111	1.1	0.82	4.579	0.78	5.22	0.02	5.22	0.06	-13	1.43	0.12
HD2021Pb1-1	1.397	3.1	9.534	8.0	0.87	4.949	5.5	9.00	0.28	9.68	0.77	171	-0.5	1.6
HD2021Pb1-2	1.365	1.8	9.318	4.6	0.88	4.950	3.2	8.80	0.16	9.46	0.43	172	-0.45	0.90
HD2021Pb1-b2	1.411	1.8	9.298	4.4	0.76	4.781	3.2	9.09	0.16	9.44	0.41	90	0.43	0.93
HD2021Pb1-c2	1.427	1.0	9.444	2.5	0.72	4.799	1.9	9.19	0.10	9.59	0.24	99	0.32	0.54
HD2021Pb1-d1	1.379	1.0	9.385	2.4	0.74	4.885	1.8	8.88	0.09	9.53	0.23	141	-0.12	0.05
HD2021Pb1-e1	1.340	1.9	9.204	4.4	0.78	4.980	3.1	8.64	0.17	9.35	0.41	186	-0.58	0.95
HD2029Pb1-1	1.356	1.4	8.835	4.7	0.47	4.727	4.2	8.73	0.12	8.98	0.42	63	0.75	0.67
HD2029Pb2-1	1.452	1.6	9.692	1.7	0.95	4.843	0.57	9.35	0.15	9.84	0.17	120	0.06	0.84

Table 2: (Continued)

Subsample Name	^{206}*Pb/ ^{238}U[a] (E-3)	Error (%)	^{207}*Pb/ ^{235}U[a] (E-3)	Error (%)	Rho[b] 6/8-7/5	^{207}Pb*/ ^{206}Pb*[a] (E-2)	Error (%)	^{206}Pb*/ ^{238}U Age (Ma)[c]	Error (Ma)	^{207}Pb*/ ^{235}U Age (Ma)[d]	Error (Ma)	^{207}Pb*/ ^{206}Pb* Age (Ma)[c]	^{234}U/ ^{238}U$_{ini}$[e]	Error
HD2054Pb1	0.576	0.54	3.890	1.4	0.75	4.899	1.1	3.71	0.02	3.99	0.06	148	0.66	0.11
HD2055Pb2	0.226	0.64	0.534	4.6	0.28	1.714	4.5	1.46	0.01	0.59	0.03	-3378	5.21	0.25
HD2055Pb3-1	1.088	0.39	4.890	1.5	0.39	3.260	1.4	7.01	0.03	5.00	0.07	-910	7.15	0.15
HD2055Pb3-2	0.498	0.56	3.217	1.60	0.50	4.681	1.4	3.21	0.02	3.31	0.05	40	1.18	0.10
HD2059Pb1-1	0.908	1.7	4.997	1.7	0.99	3.990	0.20	5.85	0.10	5.11	0.09	-357	3.56	0.55
HD2059Pb1-2	0.946	0.28	5.156	0.35	0.81	3.954	0.21	6.09	0.02	5.27	0.02	-381	3.79	0.10
HD2059Pb2	0.547	0.34	3.461	0.77	0.77	4.592	0.55	3.52	0.01	3.56	0.03	-6	1.36	0.07
HD2074UPb1	1.476	12	7.959	43	0.44	3.911	39	9.5	1.1	8.0	3.5	-409	6	6
HD2074UPb3-1	1.063	4.4	6.986	11	0.84	4.766	7.6	6.85	0.30	7.12	0.76	82.4	0.5	1.7
HD2074UPb4-1	0.806	3.5	4.860	9.8	0.82	4.373	7.3	5.19	0.18	4.97	0.48	-126	1.9	1.0
HD2074UPb5	0.887	0.8	5.186	1.6	0.60	4.239	1.3	5.72	0.05	5.30	0.08	-203	2.50	0.28
HD2074UPb7	0.889	2.8	5.255	6.4	0.55	4.288	5.4	5.73	0.16	5.36	0.34	-174	2.36	0.91
HD2074UPb8	0.894	4.8	5.309	10	0.54	4.309	8.6	5.76	0.27	5.42	0.55	-162	2.3	1.6
HD2074UPb11a	0.192	5.7	0.453	36	0.33	1.708	35	1.24	0.07	0.51	0.17	-3398	4.60	0.29
HD2093Pb1	1.515	5.9	9.570	15	0.76	4.583	11	9.76	0.58	9.70	1.50	-11	1.5	3.3
HD2238Pb1	1.460	8.7	7.391	33	0.68	3.671	28	9.41	0.82	7.50	2.40	-577	7	5
HD2247APb1	0.919	0.47	3.875	1.3	0.51	3.059	1.1	5.92	0.03	3.97	0.05	-1099	6.83	0.16
HD2257Pb1-1	0.921	1.2	5.556	2.7	0.55	4.374	2.3	5.94	0.07	5.67	0.15	-125	2.2	0.4
HD2257Pb1-2	1.562	2.7	8.839	7.5	0.56	4.103	6.4	10.1	0.27	8.98	0.67	-285	4.5	1.5
HD2257Pb1-3	1.415	5.3	6.725	15	0.45	3.447	14	9.11	0.48	6.8	1.0	-751	7.9	2.7
HD2257Pb2	1.160	1.9	7.602	4.1	0.58	4.751	3.3	7.48	0.14	7.74	0.31	75	0.71	0.82
HD2257Pb3	0.812	6.6	6.907	13	0.75	6.166	8.9	5.23	0.34	7.04	0.91	662	-3.7	2.0
HD2257Pb4	0.985	3.5	7.647	7.3	0.76	5.629	5.1	6.35	0.22	7.78	0.56	464	-2.6	1.3
HD2257Pb5	1.162	7.2	8.598	15	0.79	5.368	11	7.49	0.54	8.7	1.3	358	-2.1	3.0
HD2257Pb6	1.245	2.0	8.708	4.6	0.75	5.071	3.4	8.02	0.16	8.85	0.40	228	-0.9	0.9
HD2257Pb7[g,h]	2.513	7.6	15.111	21	0.76	4.362	16	16.2	1.23	15.3	3.2	-132	4	7
HD2260-Pb1	1.093	1.2	7.775	2.3	0.61	5.160	1.8	7.04	0.08	7.91	0.18	268	-1.15	0.47

Table 2: (Continued)

Subsample Name	^{206}*Pb/ ^{238}U[a] (E-3)	Error (%)	^{207}*Pb/ ^{235}U[a] (E-3)	Error (%)	Rho[b] 6/8-7/5	^{207}Pb*/ ^{206}Pb*[a] (E-2)	Error (%)	^{206}Pb*/ ^{238}U Age (Ma)[c]	Error (Ma)	^{207}Pb*/ ^{235}U Age (Ma)[d]	Error (Ma)	^{207}Pb*/ ^{206}Pb* Age (Ma)[c]	^{234}U/ ^{238}U$_{ini}$[e]	Error
HD2357Pb1	0.553	0.40	2.398	0.82	0.65	3.147	0.64	3.56	0.01	2.48	0.02	-1014	4.39	0.08
HD2357Pb2	0.548	0.63	2.578	1.0	0.67	3.411	0.74	3.53	0.02	2.66	0.03	-781	3.79	0.13
HD2357Pb3	0.851	0.45	4.926	0.69	0.68	4.199	0.51	5.48	0.02	5.04	0.03	-227	2.58	0.14
HD2357Pb4	0.736	0.63	3.706	1.6	0.49	3.654	1.4	4.74	0.03	3.80	0.06	-591	3.98	0.17
HD2357Pb5	0.842	5.2	4.057	15	0.45	3.493	13	5.43	0.28	4.16	0.60	-713	4.9	1.6
HD2357Pb6	0.771	2.7	4.582	6.2	0.52	4.313	5.4	4.97	0.13	4.69	0.29	-160	2.10	0.75
HD2357Pb7-1	0.320	2.4	1.798	5.4	0.53	4.070	4.6	2.06	0.05	1.87	0.10	-306	1.87	0.27
HD2357Pb7-2	0.263	9.3	1.580	21	0.51	4.364	18	1.69	0.16	1.65	0.34	-131	1.44	0.86
HD2357Pb8	0.434	8.1	2.156	43	0.49	3.600	40	2.80	0.23	2.23	0.94	-631	2.9	1.2
HD2357Pb9	0.738	1.2	4.543	2.7	0.54	4.463	2.3	4.76	0.06	4.65	0.12	-76	1.62	0.32
HD2357Pb10	0.715	3.9	4.545	13	0.59	4.608	11	4.61	0.18	4.65	0.58	1.99	1.2	1.0
HD2357Pb11	0.961	0.52	5.573	1.1	0.66	4.207	0.89	6.19	0.03	5.69	0.06	-222	2.74	0.18
HD2357Pb12	1.041	0.64	5.614	1.8	0.73	3.909	1.4	6.71	0.04	5.73	0.10	-410	4.10	0.24
HD2357Pb13-1	1.160	2.0	5.419	6.9	0.53	3.389	6.1	7.47	0.15	5.53	0.38	-799	6.83	0.85
HD2357Pb13-2	1.197	2.6	6.047	7.4	0.48	3.665	6.6	7.71	0.20	6.17	0.45	-582	5.7	1.1

[a] Isotopic ratios, corrected for mass-discrimination, spike contribution, procedure blank, and initial common lead.

[b] Error correlation between ^{207}Pb*/^{235}U and ^{206}Pb*/^{238}U.

[c] Conventional ages calculated assuming initial radioactive equilibrium.

[d] Disequilibrium ^{207}Pb*/^{235}U age calculated assuming zero initial activity of ^{231}Pa and ^{227}Ac.

[e] Initial activity ratio calculated from ^{207}Pb*/^{235}U disequilibrium age and measured ^{206}Pb*/^{238}U assuming closed system behavior.

[f] Calculated from two-point leachate-residue isochron.

[g] Not shown on Figure 2.

[h] Not shown on Figure 7.

n.d. - not determined

Table 3. Microstratigraphic positions and ages for silica samples from the Exploratory Studies Facility, Yucca Mountain

Subsample	*Depth of Dated Layer (mm)*	*Relative Depth* [a]	*$^{207}Pb^*/^{235}U$ Age of Layer (2 σ) (Ma)*
HD2019A, total thickness 9.3 mm			
Pb1	1.3	0.14	1.41 (0.81)
Pb3	5.0	0.54	4.3 (1.4)
Pb4	8.3	0.89	7.67 (0.25)
HD2019A1, total thickness 13.6 mm			
Pb1	11.3	0.83	5.95 (0.05)
Pb2	6.4	0.47	4.71 (0.05)
Pb3-1,2,3	5.24	0.39	3.92 (0.03)[b]
Pb4	1.9	0.14	1.19 (0.06)
HD2019, total thickness 30 mm			
U5	0.10	0.00	0.10 (0.01)[c]
Pb1	17.0	0.57	4.51 (0.09)
Pb2	16.0	0.53	4.33 (0.09)
Pb3-1	27.0	0.90	6.97 (0.12)
Pb3-3	27.0	0.90	5.22 (0.06)
HD2021, total thickness 12.6 mm			
Pb1-b2	12.1	0.96	9.44 (0.41)
Pb1-c2	12.1	0.96	9.59 (0.24)
Pb1-d1	11.1	0.88	9.53 (0.23)
Pb1-e1	9.6	0.76	9.35 (0.41)
HD2055, total thickness 12 mm			
Pb1	0.00	0.00	0.170 (0.032)[d]
Pb2	1.0	0.08	0.59 (0.03)
Pb3-1	10	0.83	5.00 (0.07)
Pb3-2	10	0.83	3.31 (0.05)
HD2059, total thickness 18.3 mm			
Pb3	0.1	0.01	0.341 (0.042)[d]
Pb2	8.3	0.45	3.56 (0.03)
Pb1-1,2	12.5	0.68	5.19 (0.05)[b]
HD2074, total thickness 36.7 mm			
UPb1	35.0	0.95	8.0 (3.5)
UPb3-1	31.2	0.85	7.12 (0.76)
UPb4-1	28.8	0.79	4.97 (0.48)
UPb5	27.0	0.74	5.30 (0.08)
UPb7	24.8	0.68	5.36 (0.34)
UPb8	21.2	0.58	5.42 (0.55)
UPb11a	0.20	0.005	0.51 (0.17)
HD2357, total thickness 23.0 mm			
Pb1	0.52	0.02	2.48 (0.02)
Pb2	1.68	0.07	2.66 (0.03)
Pb3	4.52	0.20	5.04 (0.03)
Pb4	3.62	0.16	3.80 (0.06)
Pb5	4.91	0.21	4.16 (0.60)
Pb6	6.98	0.30	4.69 (0.29)
Pb7-1	5.94	0.26	1.87 (0.10)
Pb7-2	5.94	0.26	1.65 (0.34)
Pb8	6.20	0.27	2.23 (0.94)
Pb9	10.3	0.45	4.65 (0.12)
Pb10	12.9	0.56	4.65 (0.58)
Pb11	11.6	0.51	5.69 (0.06)
Pb12	14.0	0.61	5.73 (0.10)
Pb13-1	15.8	0.69	5.53 (0.38)
Pb13-2	15.8	0.69	6.17 (0.45)
HD1838, total thickness 30.0 mm			
e	24.7	0.82	6.4 (0.6)
f	21.67	0.72	5.3 (3.2)[e]
g	20	0.67	9.8 (3.4)[e]
h	19.3	0.64	3.93 (0.17)
j	16.3	0.54	3.89 (0.06)
l	15.3	0.51	3.64 (0.11)
n	12.7	0.42	3.87 (0.11)
p	11.0	0.37	3.75 (0.08)
t-1,2	4.00	0.13	3.17 (0.05)[b]
v	1.33	0.04	3.13 (0.05)
HD2257, total thickness 13.0 mm			
Pb1-1	0.70	0.05	5.67 (0.15)
Pb1-2	0.70	0.05	8.98 (0.67)
Pb1-3	0.70	0.05	6.8 (1.0)
Pb2	5.70	0.44	7.74 (0.31)
Pb3	12.3	0.95	7.04 (0.91)
Pb4	10.7	0.82	7.78 (0.56)
Pb5	9.07	0.70	8.7 (1.3)
Pb6	6.74	0.52	8.85 (0.40)

[a] Distance from the sampled layer to the outer surface of the coating divided by its total thickness

[b] Average age for a subsample where ages for splits were within error limits

[c] $^{230}Th/U$ age from Paces et al. (2000)

[d] Data from Neymark et al. (2000)

[e] Unreliable ages because of low U concentrations and $^{207}Pb/^{204}Pb$ in the subsamples.